scientific reports

Check for updates

OPEN

Investigate the binding of pesticides with the TLR4 receptor protein found in mammals and zebrafish using molecular docking and molecular dynamics simulations

Sandeep Yadav[1,2,8], Mohd. Aslam[1,2,8], Ayushi Prajapat[1,7,8], Iona Massey[1,3,8], Bhaskara Nand[1], Durgesh Kumar[4], Kamlesh Kumari[5]✉, Garima Pandey[2], Chandrabhan Verma[6], Prashant Singh[1]✉ & Akram AlFantazi[6]✉

The widespread use of pesticides poses significant threats to both environmental and human health, primarily due to their potential toxic effects. The study investigated the cardiovascular toxicity of selected pesticides, focusing on their interactions with Toll-like receptor 4 (TLR4), an important part of the innate immune system. Using computational tools such as molecular docking, molecular dynamics (MD) simulations, principal component analysis (PCA), density functional theory (DFT) calculations, and ADME analysis, this study identified C160 as having the lowest binding affinity (-8.2 kcal/mol), followed by C107 and C165 (-8.0 kcal/mol). RMSD, RMSF, Rg, and hydrogen bond metrics indicated the formation of stable complexes between specific pesticides and TLR4. PCA revealed significant structural changes upon ligand binding, affecting stability and flexibility, while DFT calculations provided information about the stability, reactivity, and polarity of the compounds. ADME studies highlighted the solubility, permeability, and metabolic stability of C107, C160, and C165, suggesting their potential for bioavailability and impact on cardiovascular toxicity. C107 and C165 exhibit higher bioactivity scores, indicating favourable absorption, metabolism, and distribution properties. C165 also violated rule where molecular weight is greater than 500 g/mol. Further, DFT and NCI analysis of post MD conformations confirmed the binding of ligands at the binding pocket. The analysis shed light on the molecular mechanisms of pesticide-induced cardiovascular toxicity, aiding in the development of strategies to mitigate their harmful effects on human health.

Keywords Pesticides, Cardiovascular toxicity, Toll-like receptor 4 (TLR4), Molecular docking, Molecular dynamics simulations, 3FXI

Pesticides are extensively used in agriculture to protect crops against parasites and enhance agricultural yield[1]. Nevertheless, their widespread use poses notable hazards to both human health and the environment[2]. Exposure to pesticides can cause severe toxicities like neurotoxicity[3], cardiotoxicity[4], genotoxicity[5], embryotoxicity[6] etc. Among them, cardiovascular toxicity stands out as a major concern due to its potentially severe outcomes. Numerous studies have linked pesticides to the growth of diseases related to heart and blood such as hypertension,

[1]Department of Chemistry, Atma Ram Sanatan Dharma College, University of Delhi, Delhi, India. [2]Department of Chemistry, Faculty of Engineering and Technology, SRM Institute of Science and Technology, Delhi-NCR Campus, Modinagar, Ghaziabad, Uttar Pradesh, India. [3]Amity Institute of Biotechnology, Amity University, Noida, India. [4]Department of Chemistry, Maitreyi College, University of Delhi, Delhi, India. [5]Department of Zoology, University of Delhi, Delhi-110007, India. [6]Department of Petroleum and Chemical Engineering, Khalifa University of Science and Technology, P.O. Box 127788, Abu Dhabi, United Arab Emirates. [7]Department of Chemistry, University of Delhi, Delhi-110007, India. [8]Sandeep Yadav, Mohd. Aslam, Ayushi Prajapat, Iona Massey: Equal authorship ✉email: kkumari@zoology.du.ac.in; psingh@arsd.du.ac.in; kram.alfantazi@ku.ac.ae

atherosclerosis, and myocardial infarction[7,8]. Additionally, leveraging the unique advantages of zebrafish as a model organism for drug toxicity screening could further enhance our understanding of cardiovascular toxicity, bridging the gap between in vitro and in vivo studies. Zebrafish, with their well-developed organs and particularly their heart, offer a valuable platform for studying cardiotoxicity and its implications[9].

Wu et al. examined the immunotoxicity, developmental toxicity, and cardiotoxicity caused by methidathion, an organophosphorous pesticide, using embryonic zebrafish as a model organism. Methidathion was administered to zebrafish embryos at different concentrations. The study utilized qPCR assays to probe gene expression related to cardiac development, cellular apoptosis, and immune function to better understand the toxic effects of methidathion. Results showed a decline in zebrafish survival rate, hatchability, and length of zebrafish, along with increased abnormalities and cardiac developmental toxicity upon exposure to methidathion. Additionally, oxidative stress was triggered in the zebrafish, with apoptotic cells predominantly located in the pericardial region as indicated by acridine orange staining[10]. However, only the experimental studies were carried out in the above-reported studies The mechanism responsible for the cardiovascular toxicity induced by pesticides remained unclear. Consequently, scientists opted to investigate the toxicity using in-silico techniques. Saputra et al. investigated the cardiovascular toxicity triggered by fenpropathrin, a pyrethroid pesticide, in zebrafish voltage-gated sodium channels, using both in vivo and in silico methods. The findings showed elevated heart rate, stroke volume, cardiac output, and shortening fraction, with molecular docking studies showing a high binding affinity between the pesticide and the channels[11]. Besides these sodium channels, more receptors have been discovered as potential targets for cardiovascular toxicity by pesticides. Recently, there has been increased interest in TLR4, a key component of the innate immune system, as a potential target for cardiovascular toxicity induced by pesticides[12]. Activation of TLR4 has been linked to inflammation, oxidative stress, and endothelial dysfunction, which are central processes in the pathogenesis of cardiovascular diseases[13]. In a recent investigation, Gu et al. explored emamectin benzoate (EMB)-induced cardiovascular toxicity via Toll-like receptor pathways, resulting in inflammation, cardiac tissue apoptosis, abnormal heart function, and impaired blood vessel formation. Molecular docking and aspirin anti-inflammatory rescue assays were performed which implied potential targeting of Toll-like receptor 2 (TLR2) and Toll-like receptor 4 (TLR4) by EMB[14].

Honegr et al. conducted in silico studies to design novel ligands for TLR4 to develop new types of immunologic adjuvants. They docked a total of 10,000 compounds at the binding site of the hTLR4/MD2 complex and calculated the binding energies. The binding energies for LPS, MPLA, and Eritoran with hTLR4/MD2 were found to be − 8.7, − 7.4, and −7.3 kcal/mol, respectively[15]. In another study by the same group, virtual high-throughput screening (vHTPS) was employed to rationally design new modulators of hTLR4/MD2[16]. Likewise, Mururgueitio and colleagues examined a collection of three million compounds, discovering a few virtual hits (AG1, AG2, AG3, AG4) that boosted NF-kB activation induced by the lipopeptide ligand Pam3CSK4 in luciferase reporter assays using HEK293-TLR2 cells[17]. Additionally, Farhadi et al. utilized in silico methods to design derivatives of flagellin as potential adjuvant candidates and investigated their interactions with TLR5[18]. Similarly, Švajger et al. performed both structural and ligand-based virtual screening targeting the TLR4–MD2 interface. They identified three hit compounds with promising TLR4 antagonistic activities, demonstrating micromolar IC_{50} values and the ability to suppress cytokine secretion in human peripheral blood mononuclear cells[19]. TLR4 agonists are particularly valuable as adjuvants in cancer immunotherapy and vaccines, such as the hepatitis B (Fendrix) and cervical cancer (Cervari) vaccines, which utilize synthetic, non-toxic lipopolysaccharide (LPS) analogues[20,21]. Studies have focused on developing the inhibitors of TLR4 using PDB 3FXI[22–25] and learn about its mechanism[26]. Further, various cardiovascular studies have used 3FXI to study the effect on TLR4[27,28].

Although there is increasing evidence suggesting the involvement of TLR4 in pesticide toxicity, the specific molecular interactions and the stability between pesticides and TLR4 are yet unknown. Hence, it is crucial to understand the molecular interactions occurring between pesticides and the TLR4 receptor, as well as identify the pesticides responsible for inducing a greater amount of toxicity.

Since there are limited studies employing in-silico approaches to assess the cardiovascular toxicity induced by pesticide binding on the TLR4 receptor protein found in both mammals and zebrafish. The work herein aims to screen a vast library of pesticides for their potential cardiovascular toxicity in zebrafish receptor TLR4. Advanced computational techniques, including molecular docking, molecular dynamics (MD) simulations, principal component analysis (PCA), and density functional theory (DFT) calculations along with absorption, distribution, metabolism, and excretion (ADME) studies were employed. By elucidating the binding modes and dynamics of pesticides with TLR4, this study will gain a deeper understanding of the underlying mechanism behind pesticide-induced cardiovascular toxicity. This comprehensive approach allows for a systematic assessment of pesticide toxicity, offering valuable insights for risk evaluation and the development of targeted intervention strategies.

Computational calculations

Library preparation

The list of pesticides mentioned **Table S1** was obtained from an online website https://www.fao.org/fao-who-codexalimentarius/codex-texts/dbs/pestres/pesticides/en/ and their chemical structures were procured from ChemSpider[29].

Protein preparation and active site prediction

The protein sequence for Toll-like receptor 4 (PDB ID: 3FXI) was procured from the RCSB protein data bank (https://www.rcsb.org/structure/3FXI). The protein was obtained and prepared utilizing AutoDock Tools software[30]. The preparation process consisted of eliminating undesirable water molecules and associated ligands and subsequently introducing polar hydrogens and Gasteiger charges. In addition, the protein that had been

prepared was analyzed using Discovery Studio Visualizer[31] which allowed for the identification of the possible binding site. To determine the binding pocket/region for molecular docking, the PDB file was first opened in Discovery Studio Visualizer. Within the receptor-ligand interactions section, the "Define and Edit Binding Site" option was utilized from the left-side panel. This tool allows for the selection of receptor cavities, PDB site records, or any ligand to define the binding site.

The binding site's dimensions were determined to be (x = 4.517 Å), (y = 0.918 Å), and (z = 20.14 Å). The box dimensions were (51 Å x 51 Å x 51 Å). Figure 1 contains an image of the active site region of TLR4.

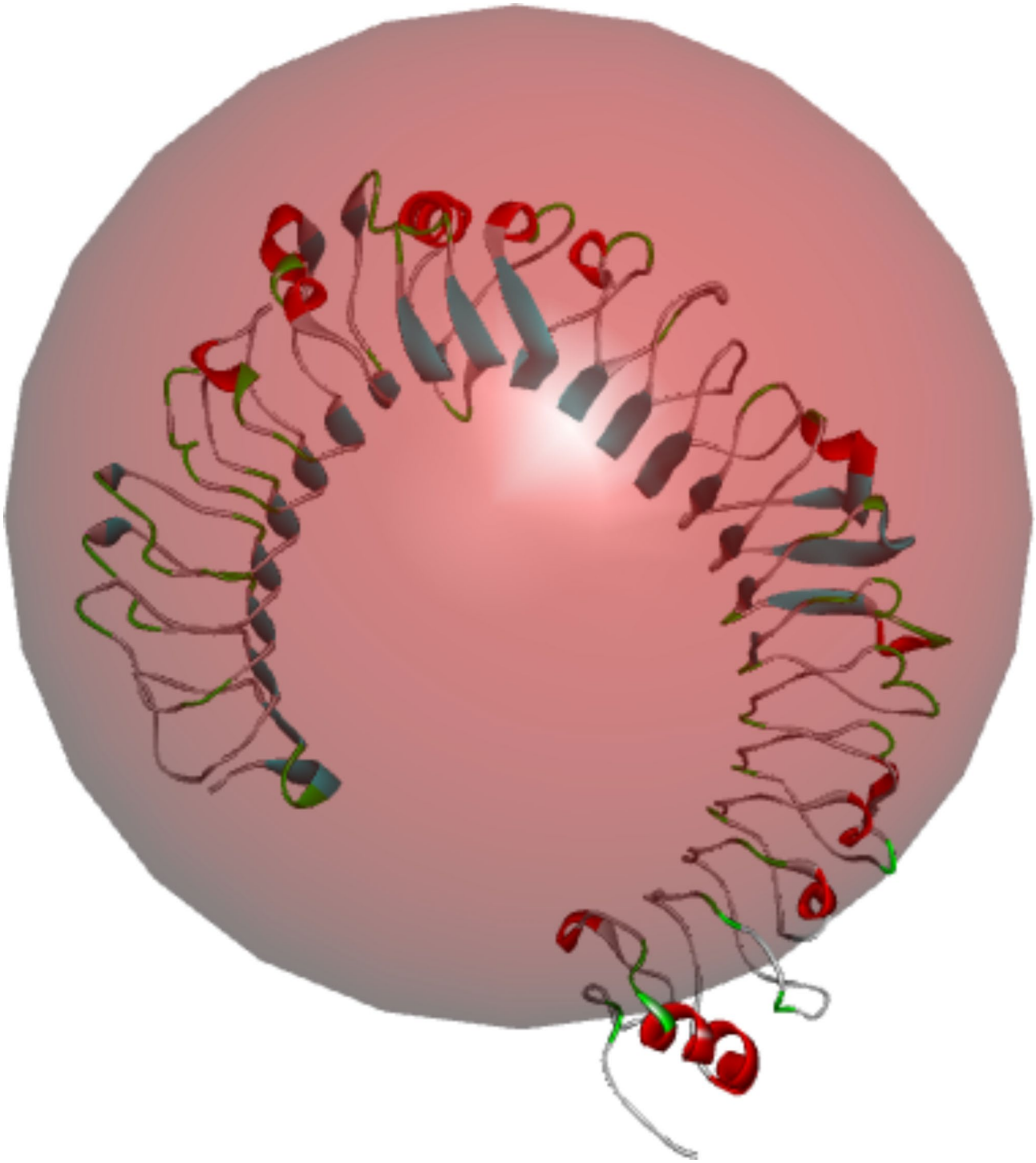

Fig. 1. Binding pocket of 3FXI.

Molecular docking

Docking was performed using AutoDock Tools. Multiple ligand docking was performed with a diverse ligand library. Initially, a file comprising all ligands was created, followed by a configuration file consisting of necessary docking variables for the protein-ligand interaction was generated. Perl scripting is supported by AutoDock Vina for script-based docking and analysis, facilitating the automation of tasks such as protein and ligand preparation, docking simulations, and result analysis. The docking process was automated by executing a Vina Perl script that incorporated the configuration file through the command prompt. In addition, a 2D map of the protein-ligand combination with the highest binding energies was created using Discovery Studio Visualizer.

Molecular dynamics (MD) simulations

MD simulations of only protein and protein-ligand complex were done using GROMACS. The standard force field used was CHARM27. At first, a topology file was created using SwissParam http://www.swissparam.ch/, and then Ubuntu Linux was used for further steps of simulations. Solvation was done using the TIP3P water model within a triclinic box. The ions that corresponded to the system were introduced, and the steepest descent algorithm was used to conduct energy reduction. Every simulation was conducted for a total of 50,000 steps. Further, equilibration was done using NVT and NPT for 100 ps at 300 K each. Initially, the MD simulations were run for 100 ns and then for 300 ns.

Principal component analysis (PCA)

The files generated from md simulations was first centered and then converted to trajectory files for performing PCA analysis. This analysis was implemented in a two-step process i.e. constructing the covariance matrix and then diagonalizing the resulting matrix. The 'gmx covar' command was initially used to calculate the covariance matrix and principal vectors. Subsequently, the 'gmx anaeig' program was employed to generate the principal component data. The movement of both protein and complexes was analysed by projecting the initial two eigenvectors (ev1 vs. ev2), which represented the most important motions.

Density functional theory (DFT) calculations

Gaussian 16 was used to perform DFT calculations of the ligands with least binding affinity. The job type selected was optimization and frequency. DFT calculations utilizing B3LYP method were employed for geometry optimization and frequency analysis. The basis set used here was 6-311G. The symmetry was ignored, quadratically convergent SCF was used, and solvation was kept at default. Finally, the task was submitted, initiating the DFT calculations.

Determination of ADME properties

ADME is an abbreviation of Adsorption, Digestion, Metabolism, and Excretion. ADME was employed to obtain the physicochemical properties of the ligands. For this, Swiss ADME server http://www.swissadme.ch/ was employed in which the smiles of the desired ligand were uploaded to get the results (Fig. 2).

Results and discussion

Molecular docking analysis and interaction maps of pesticides with TLR4

Molecular docking is a method which is used to predict the preferred arrangement of one molecule relative to another when a ligand binds to a target protein, forming a stable complex[32]. Scoring functions, such as knowledge of the preferred orientation, can be utilized to predict the binding affinity or the degree of association strength between two molecules[33,34]. The binding energies of different pesticides (ligands) with the protein TLR4 are presented in Table 1. C107, C160 and C165 showed the best binding with TLR4 with binding affinities of -8.0, -8.2 and −8.0 kcal/mol respectively, based on the scores these three molecules were selected for further analysis.

The two-dimensional (2D) interactions of TLR4 with C107 are shown in Fig. 3a. Hydrogen bonds were formed exclusively by the amino acid residues ASP453_3.37 and THR459_3.16. ILE454_3.11 is the only amino acid residue which forms π -sigma bond. The amino acid residues that displayed halogen bonding interactions, along with their corresponding distances, are as follows: ASN433_0.97/1.72/3.58, SER432_3.53/2.52, THR457_2.06/3.12, ASP453_2.33, LEU452_2.65, HIS426_3.08, LEU427_2.94/1.37, LEU434_1.86/1.95/3.67. Alkyl and π-alkyl bonds are being formed by LEU449_5.17 and LEU434_3.73/4.99 whereas TYR_4.51 showed π- π stacked interaction. Furthermore, the 2D interaction maps of TLR4 with C160 are represented in Fig. 3b.

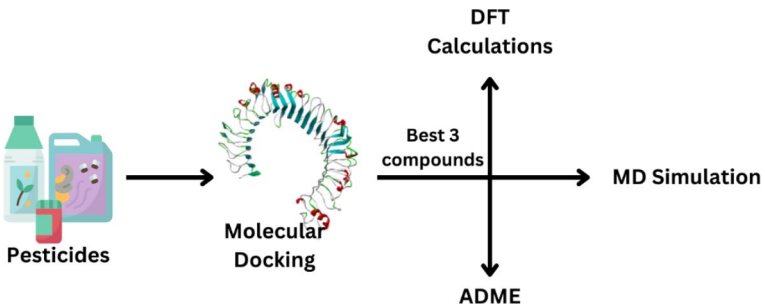

Fig. 2. Schematic flow chart of the methodology.

C.no	BE	C.no	BE	C.no	BE	C.no	BE	C.no	BE	C.no	BE	C.no	BE
1	-7.6	39	-5.0	77	-5.6	115	-6.7	153	-5.2	191	-5.3	229	-6.9
2	-4.1	40	-4.8	78	-5.8	116	-6.9	154	-4.5	192	-5.6	230	-5.8
3	-5.4	41	-5.5	79	-7.0	117	-6.0	155	-5.6	193	-5.9	231	-5.0
4	-4.9	42	-7.0	80	-3.8	118	-5.1	156	-6.1	194	-6.5	232	-5.8
5	-5.6	43	-5.4	81	-3.6	119	-4.7	157	-1.6	195	-6.9	233	-5.7
6	-7.3	44	-6.3	82	-5.8	120	-5.4	158	-5.9	196	-6.6	234	-5.4
7	-4.3	45	-5.8	83	-3.7	121	-6.6	159	-4.9	197	-6.1	235	-5.8
8	-5.5	46	-6.1	84	-6.1	122	-5.9	160	**-8.2**	198	-5.9		
9	-5.1	47	-5.8	85	-7.4	123	-7.1	161	-6.8	199	-7.3		
10	-5.6	48	-5.9	86	-6.3	124	-5.4	162	-7.3	200	-5.9		
11	-5.6	49	-6.8	87	-7.1	125	-6.0	163	-4.0	201	-5.9		
12	-7.3	50	-6.5	88	-6.4	126	-6.8	164	-5.2	202	-5.4		
13	-4.0	51	-6.7	89	-5.0	127	-6.4	165	**-8.0**	203	-5.8		
14	-6.0	52	-6.6	90	-5.9	128	-6.1	166	-4.2	204	-7.0		
15	-6.3	53	-6.0	91	-5.9	129	-5.8	167	-5.6	205	-5.4		
16	-5.7	54	-5.8	92	-5.9	130	-6.8	168	-5.4	206	-6.6		
17	-5.8	55	-5.7	93	-5.6	131	-5.9	169	-5.5	207	-6.0		
18	-7.4	56	-6.6	94	-7.3	132	-6.4	170	-5.6	208	-7.7		
19	-6.5	57	-6.1	95	-6.6	133	-6.2	171	-5.6	209	-7.5		
20	-6.2	58	-5.0	96	-6.3	134	-5.5	172	-6.4	210	-6.3		
21	-6.9	59	-4.9	97	-6.2	135	-6.3	173	-6.9	211	-5.7		
22	-7.1	60	-4.5	98	-6.4	136	-7.2	174	-4.8	212	-6.3		
23	-6.6	61	-4.5	99	-5.1	137	-5.7	175	-3.6	213	-6.1		
24	-6.7	62	-6.0	100	-6.8	138	-4.3	176	-5.7	214	-3.7		
25	-6.0	63	-5.7	101	-6.3	139	-7.0	177	-6.0	215	-5.6		
26	-5.7	64	-6.5	102	-5.5	140	-4.2	178	-6.1	216	-6.4		
27	-4.5	65	-6.7	103	-6.7	141	-5.3	179	-6.5	217	-6.9		
28	-5.9	66	-4.4	104	-7.0	142	-6.0	180	-5.8	218	-3.9		
29	-5.8	67	-5.0	105	-6.5	143	-5.3	181	-5.3	219	-6.3		
30	-6.2	68	-4.2	106	-5.3	144	-5.5	182	-5.6	220	-5.7		
31	-5.6	69	-6.3	107	**-8.0**	145	-6.0	183	-5.1	221	-5.5		
32	-5.0	70	-5.5	108	-7.6	146	-7.0	184	-5.7	222	-6.1		
33	-7.0	71	-5.4	109	-6.7	147	-7.9	185	-4.8	223	-4.7		
34	-5.6	72	-5.6	110	-6.7	148	-4.9	186	-3.9	224	-7.0		
35	-5.4	73	-5.9	111	-6.7	149	-5.3	187	-5.5	225	-5.6		
36	-3.0	74	-3.6	112	-5.8	150	-6.5	188	-5.9	226	-6.1		
37	-4.8	75	-5.9	113	-6.3	151	-3.7	189	-3.5	227	-5.3		
38	-5.8	76	-5.9	114	-6.7	152	-4.5	190	-5.3	228	-6.2		

Table 1. Binding energies obtained through molecular docking studies.

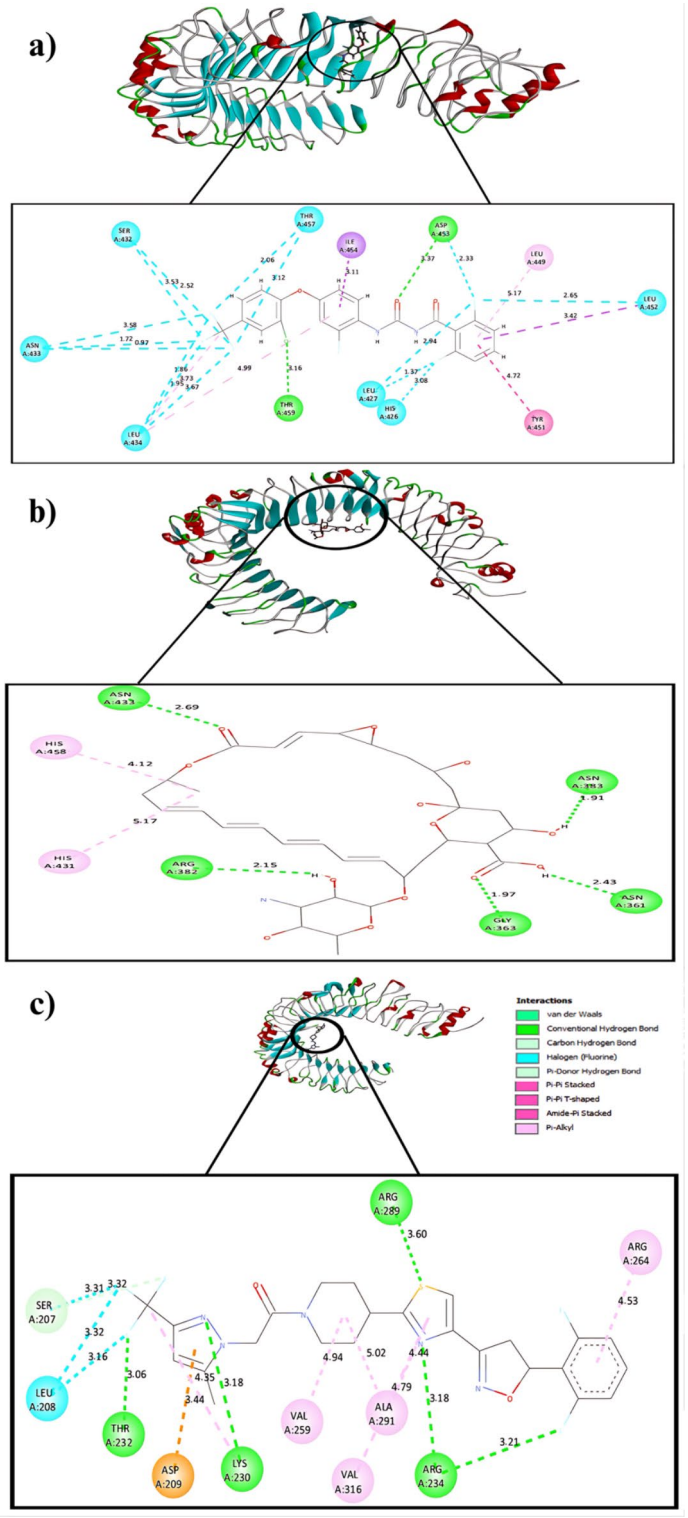

Fig. 3. 2D docked poses of (**a**) C107 with active site region of TLR4 protein, (**b**) C160 with active site region of TLR4 protein, (**c**) C165 with active site region of TLR4 protein.

Conventional hydrogen bond and π-alkyl were the two molecular interactions observed in 2D map. The amino acid residues and their distances from the ligand, involved in hydrogen bonding interactions are ARG382_2.15, ASN433_2.69, GLY363_1.97, ASN361_2.43, ASN383_1.91 whereas the residues which are involved in the formation of π-alkyl bond are HIS458_4.12, HIS431_5.17. Figure 3c displays 2D view of molecular interactions in TLR4 with C165. THR232_3.06, LYS230_3.18, ARG289_3.60 and ARG234_3.18/3.21 are exhibiting the conventional hydrogen bonding interactions. SER207_3.32 is the only residue which is showing carbon

hydrogen bonding interactions. π -anion bond formation is demonstrated by ASP209_3.44. The residues which are involved in the formation of alkyl and π-alkyl bonds are VAL259_4.94, VAL316_4.79, ALA291_5.02/4.44, ARG264_4.53. Halogen bonding interactions is shown by SER207_3.31 and LEU208_3.32/3.16.

The structural comparison of the emamectin benzoate (EMB) with the chosen pesticides, C107, C160 and C165 was done to check the similarity in their structures to identify any specific group which might be responsible for toxicity (Fig. 4). EMB and C160 exhibited most structural similarity, namely, presence of a macrocyclic ring containing ether functional group, both the structures possess tetrahydopyran in the side chains. The pesticide derivates C107 and C165 does not possess any noticeable similarities with EMB other than the fact they both are macromolecules containing heteroatoms and multiple functional groups among which carboxyl is a commonality. However, C107 and C165 structures have many similarities with each other, notably, both the structures possess CF3 substituent and difluorobenzene at the terminals along with amide group in their respective structures.

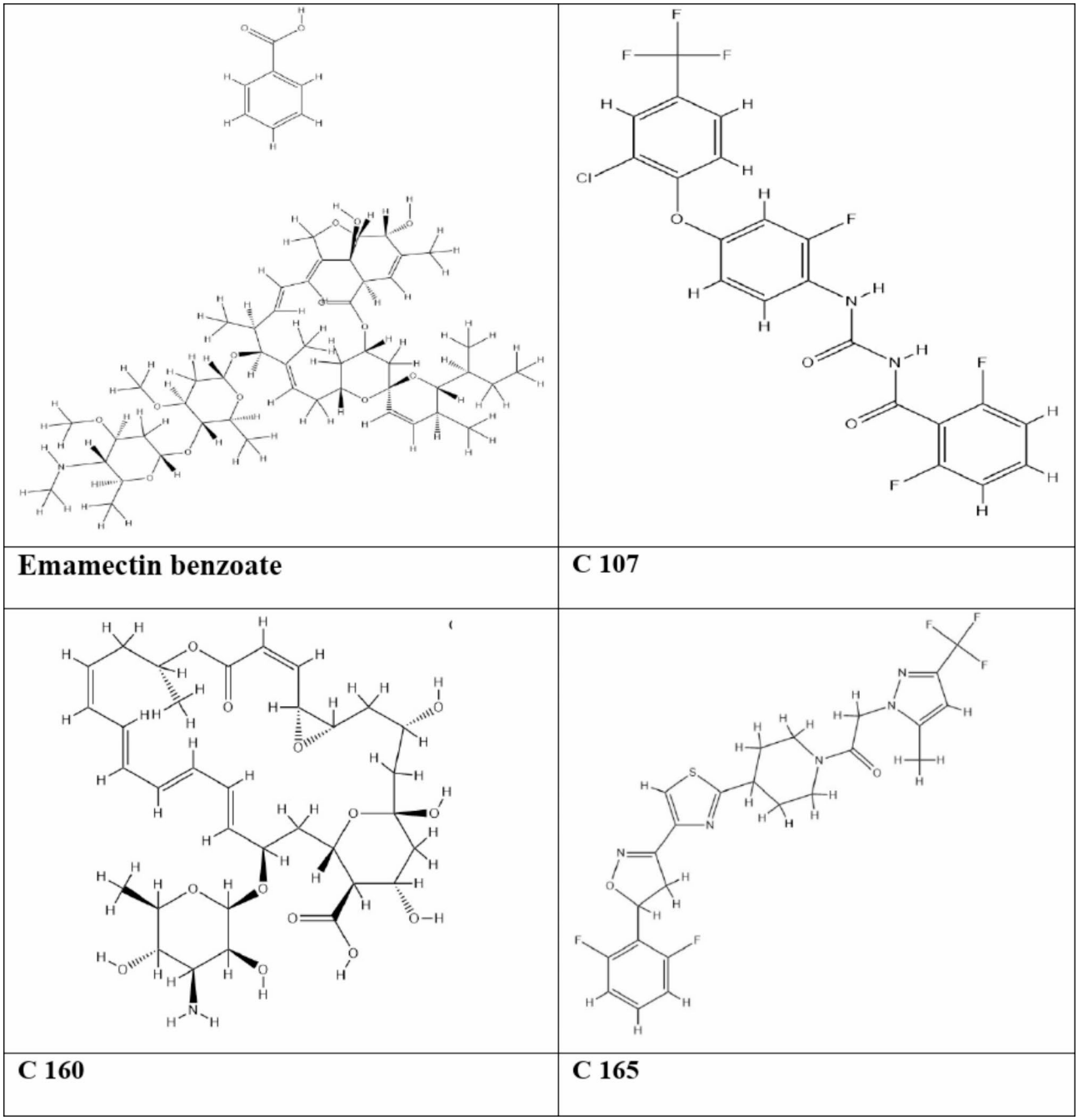

Fig. 4. 2D structures of emamectin benzoate, C107, C160 and C165.

Molecular dynamics (MD) simulations to understand the formation of the complex

100 ns simulation

RMSD, RMSF and hydrogen bond analysis MD simulations are real-time simulations extensively employed to examine the conformational changes, stability, and interactions between proteins and ligands within the complex[35]. Stability of conformational changes with nanosecond-level precision, enabling the system to illustrate atomic-level changes in terms of coordinates can be studied with MD simulations[36–38]. MD simulations were performed to analyse the stability of native protein and complex. It produces a range of trajectories, which provide a valuable understanding of protein-ligand interactions and enable further investigation of these interactions[39,40]. The different trajectories include root mean square deviation (RMSD), root mean square fluctuations (RMSF), and hydrogen bonds.

RMSD quantifies the average displacement of atoms within[41] the protein-ligand complex relative to their positions in the initial frame[42,43]. The binding of a ligand into the active site enhances the conformational stability of the macromolecular system[44]. Figure 5a represents RMSD plots of TLR4 protein bound to compounds with favourable binding affinities, namely C107, C160, and C165 (ligands). The RMSD value of the native protein was measured at 4.9 Å at 79 nanoseconds (ns). The protein exhibited the highest fluctuations during the entire simulation time. In the TLR4 and C107 complex, the highest RMSD value obtained was 5.9 Å at 26 ns, with maximum fluctuations observed until 90 ns. Subsequently, the complex began to stabilize, exhibiting fewer fluctuations. The peak RMSD value recorded for the TLR4 complexed with C160 reached 5.3 Å at 84 ns, exhibiting minimal fluctuations throughout the entire simulation period. Conversely, the TLR4 complexed with C165 exhibited its highest RMSD value of 7.4 Å at 75 ns, with fewer fluctuations observed until 65 ns. At this point, there was a sudden decrease in RMSD value, followed by a sharp rise within the time frame of 69 to 73 ns. Interestingly, all three complexes exhibited more stable fluctuations compared to the native protein.

RMSF provides insights into the fluctuation levels of individual residues across the entire structure of protein and protein-ligand complex. RMSF is a quantitative measure of how much the amino acid residue has deviated from its mean position throughout the simulation period. It offers valuable information regarding the flexibility or mobility of the residue[45]. It is usually plotted for a better understanding of residue-wise fluctuation in both protein and complex. Figure 5b illustrates RMSF plots of the native protein and the three protein-ligand complexes. The highest fluctuating residues obtained in native protein were SER563, LEU202, TYR266, GLY439 and THR585 residues with a RMSF values of 1.5 Å, 1.3 Å, 1.2 Å, 1.1 Å and 1.0 Å. In contrast, the highest fluctuating amino acid residues in TLR4 complexed with C107 were GLN562 at 1.5 Å, LEU102 at 1.4 Å ALA265 at 1.2 Å, LYS124 and LEU202 at 1.3 Å. The amino acid residues that showed maximum fluctuations in TLR4 complexed with C160 were ALA265 at 1.9 Å and GLN562 at 2.2 Å. Finally, the amino acid residues exhibiting maximum fluctuations in the complex between TLR4 and C165 were GLN562 at 2.8 Å, LEU485 at 1.7 Å and THR585 at 1.8 Å.

The radius of gyration (Rg) was calculated to assess the compactness of the macromolecules in the absence and presence of ligands. Rg refers to the radial mass-weighted distance between an atom and its centre of mass[46]. Figure 6a demonstrated Rg plots calculated for both TLR4 and TLR4 complexed with C107, C160 and C165. High Rg values during molecular dynamics simulations suggests low compactness of the protein, whereas low Rg values indicate greater compactness of the protein[47]. The maximum Rg value of the TLR4 observed was 33.2 Å at 54 ns while that of TLR4 complexed with C107, C160 and C165 were 35.4 Å at 26 ns, 33.6 Å at 24 ns and 35.9 Å at 75 ns. The native protein exhibited lower Rg value than the complexes, indicating more compactness and stability in the protein structure than the complexes. Furthermore, fewer fluctuations were observed in the complexes compared to the native protein, possibly indicating increased stability of the protein upon ligand binding.

Higher number of hydrogen bonds can be correlated to the stability of the complex (protein-ligand)[48]. Figure 6b illustrates the total count of hydrogen bonds produced by all three complexes over the whole duration of the simulation. All three complexes established a maximum of four hydrogen bonds.

Principal component analysis PCA analysis was performed to determine the conformational changes of the protein induced by ligands binding and to elucidate the collective motions within the MD trajectories[49]. It is feasible to have a deeper knowledge of how the complex develops over time and which motion patterns are most significant by examining the PCA findings at each time point. Each point on the plot represents a snapshot from the MD trajectory projected onto the first two principal components (eigenvectors), which capture the most significant collective motions. According to Fig. 7, the native protein occupied a small phase space with a compact cluster, suggesting limited conformational variability and good stability in the absence of ligand. However, it was observed that upon ligand binding, the phase space increased and the structure became more flexible. Moreover, there was also a difference in phase space when all the three complexes were compared. Among all the three complexes, TLR4-C107 demonstrated a relatively tighter cluster, indicating less structural variation and more stability upon binding with C107 as shown in Fig. 7b whereas TLR4 bound with C165 was shown to occupy the largest phase space exhibiting highest structural variation and flexibility, indicating minimal stability as represented in Fig. 7d. The TLR4 and C160 complex indicated that their binding significantly increases the conformational space occupied by the protein and the principal components were distributed broadly as displayed in Fig. 7c. TLR4-160 complex was an intermediate between both the above complexes in terms of phase space, structural variation, and stability. This means it was neither too compact nor flexible and no major structural variations were observed. From this it can be said that the native protein upon binding with different ligands underwent major structural variations making the structure less compact, less stable and more flexible.

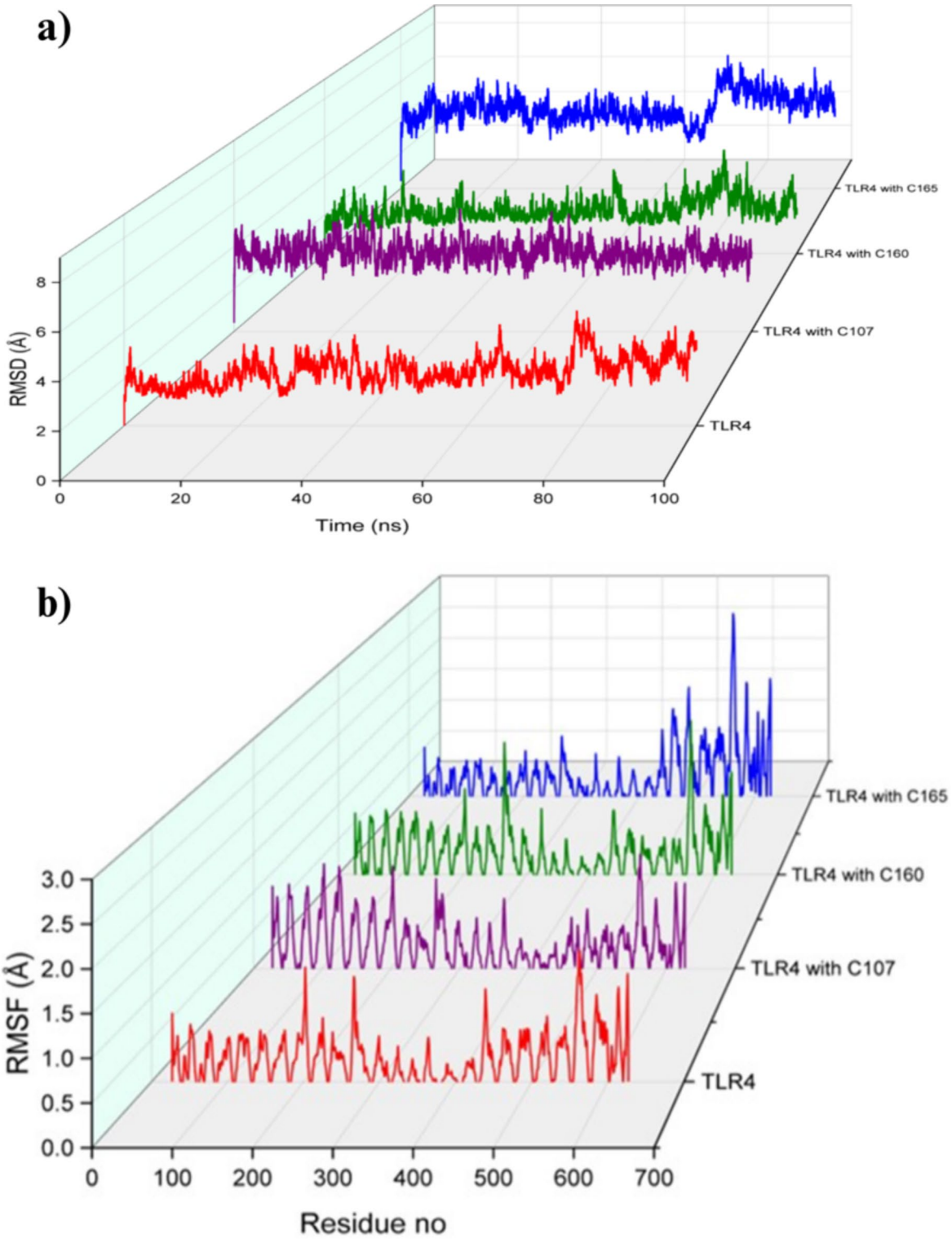

Fig. 5. (**a**) RMSD and (**b**) RMSF obtained from the trajectories of 100ns simulations.

MD simulations for 300 ns

Ther RMSD and RMSF analyses from the 300 ns molecular dynamics (MD) simulations of the 3FXI protein with Flufenoxuron (107), Natamycin (160), and Oxathiapiprolin (165) reveal significant insights into the stability and flexibility of these complexes. The RMSD plots (Fig. 8a) indicate that all three complexes reach equilibrium after an initial adjustment period, with the 3FXI-Flufenoxuron complex showing the highest RMSD values, suggesting greater structural fluctuations. In contrast, the 3FXI-Natamycin and 3FXI-Oxathiapiprolin complexes exhibit lower RMSD values, indicating more stable interactions. The RMSF plots (Fig. 8b) further

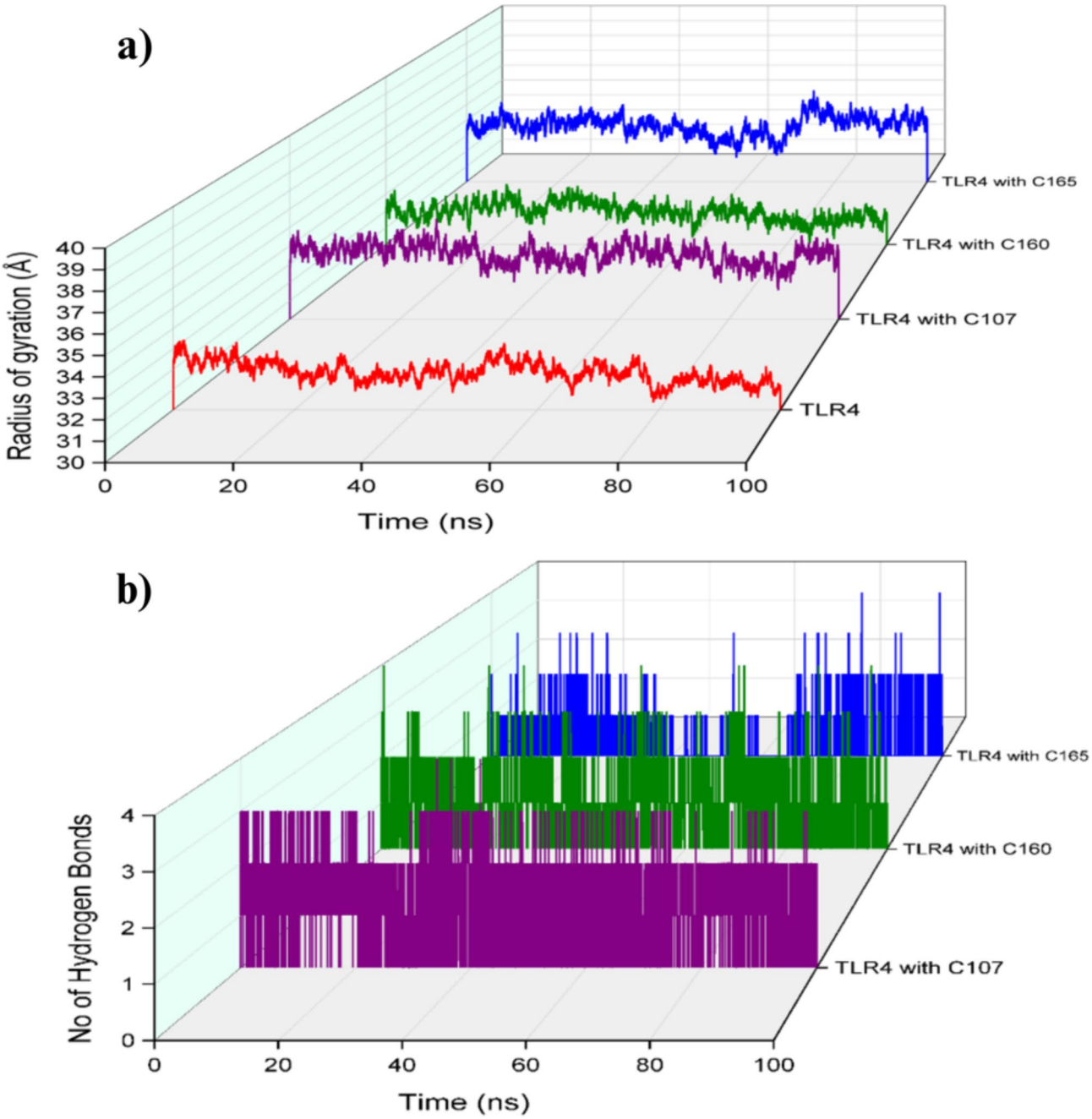

Fig. 6. (**a**) Radius of gyration analysis plots of TLR4 with C106, C160 and C165. (**b**) Number of hydrogen bonds formed during 100 ns simulations.

supports these findings, showing reduced fluctuations in the binding site regions for all three ligands, with the 3FXI-Oxathiapiprolin complex displaying the least fluctuation, suggesting a more rigid and stable interaction at the binding site.

The analysis of hydrogen bond number and Rg provides additional information about the stability and compactness of the protein and protein-ligand complexes. Figure 9a contains the plots of hydrogen bond number between ligands and the protein. The 3FXI-Natamycin complex have the most number of hydrogen bonds, correlating with its lower RMSD and Rg values, indicating a stable and tightly bound complex. The 3FXI-Oxathiapiprolin complex also shows a significant number of hydrogen bonds, resulting into increased stability. The Rg values for all three complexes remain relatively stable throughout the simulation (Fig. 9b), with the 3FXI-Natamycin complex showing a slightly lower Rg value, suggesting a more compact structure. These findings highlight the importance of hydrogen bonding in stabilizing the complexes and provides important information about the dynamic behaviour of these protein-ligand interactions.

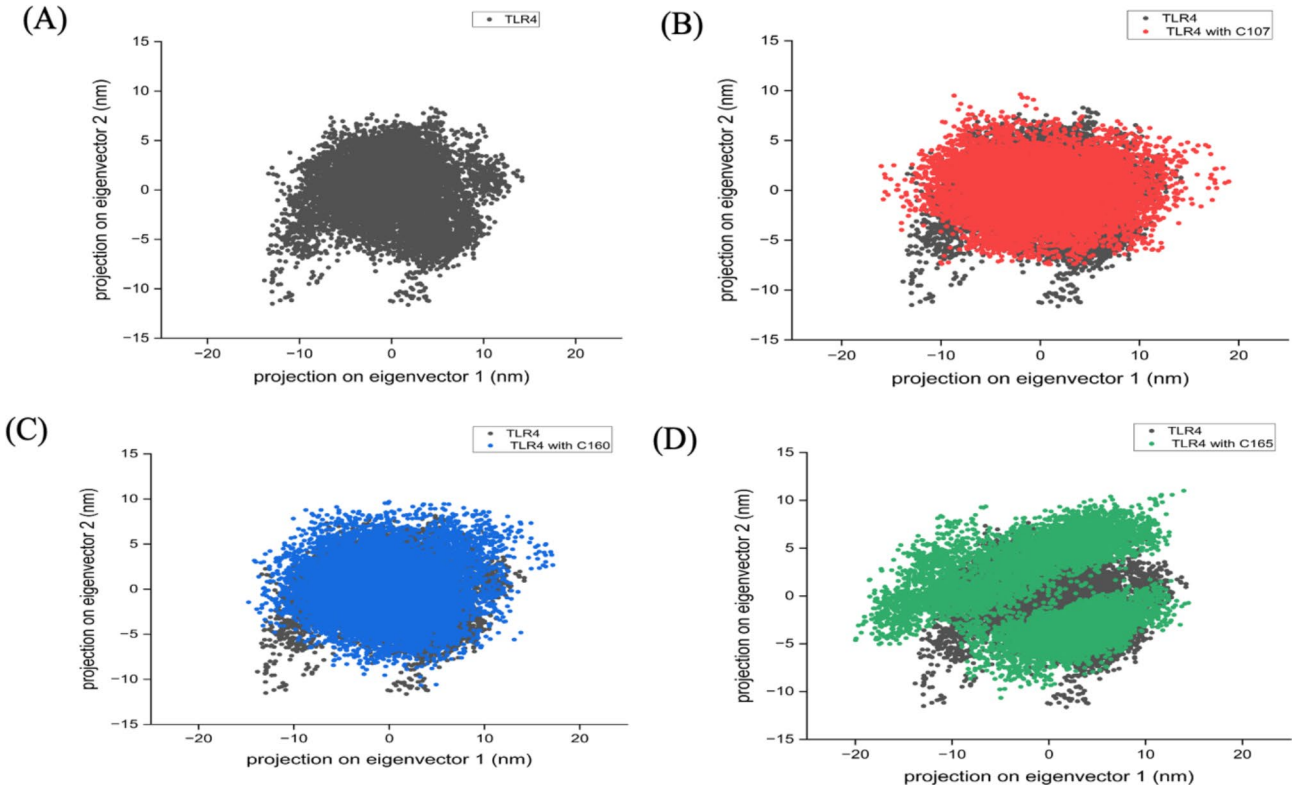

Fig. 7. illustrates PCA analysis of (**a**) TLR4 protein and TLR4 complexed with (**b**) C107 (**c**) C160 (**d**) C165.

Pre- and post-MD comparison of docked ligand

Docked pose analysis Comparing the docked ligand in the protein before and after MD simulations provides valuable insights into conformational changes and interaction dynamics. The Fig. 10 presents a surface view of the TLR4 binding cavity with the superimposed conformations of the selected molecules (C107, C160, and C165) from both the molecular docking and MD simulation analyses. The figure clearly illustrates how each ligand fits within the active site.

2D and 3D representations of docked and MD poses of C107, C160 and C165 with 3FXI are present in Fig. 11. For the ligand C107, the docking interactions included THR A:457, SER A:432, ASP A:453, ILE A:454, LEU A:449, and ASN A:433. After 300 ns of MD simulation, the interactions with ASP A:453, LEU A:427, and THR A:457 were retained, indicating stable binding. New interactions with GLU A:425, LEU A:446, and PHE A:418 emerged, suggesting a shift in the binding pose. The types of interactions observed include conventional hydrogen bonds (green) and pi-alkyl interactions (pink).

For the ligand C160, the docking interactions included ASN A:433, HIS A:458, HIS A:431, ARG A:382, TYR A:451, ASN A:383, and GLY A:363. Post-MD simulation, the interaction with ARG A:382 was maintained, while new interactions with GLY A:384, GLY A:410, and PHE A:408 were observed. This indicates a partial retention of the original binding interactions with some reorientation. For the ligand C165, the docking interactions included ARG A:289, ASN A:361, ARG A:264, SER A:207, LEU A:208, VAL A:259, ALA A:291, ASP A:209, LYS A:230, VAL A:316, and ARG A:234. After 300 ns MD simulation, the interactions with ILE A:454, LEU A:434, and THR A:457 were retained, while new interactions with PHE A:443, VAL A:442, and MET A:437 emerged. This suggests a stable binding with additional interactions forming over the simulation period.

Hydrogen bond occupancy Hydrogen bond occupancy was calculated from the 300 ns trajectories, with the results detailed in Table 2. For compound C107, the hydrogen bond occupancy data reveals that the interactions between the side chain of LIG628 and the main chain of GLU425, with an occupancy of 4.10%, has significant contribution to the stability. This interaction likely plays a key role in stabilizing the ligand within the binding site. Other interactions, such as the THR457-Side to LIG628-Side (1.10%) and ASP453-Main to LIG628-Side (0.75%), are moderately significant but less critical compared to the GLU425 interaction. The remaining hydrogen bonds, including those between the main chains of LEU427, LEU434, and HIS426 with LIG628, show much lower occupancies (ranging from 0.15 to 0.30%), suggesting they contribute minimally to the overall stability of the compound within the binding site.

Compound C160 exhibits the strongest and most numerous hydrogen bond interactions among the three compounds analyzed. The most prominent interaction is between ARG382 and the side chain of LIG628, with an exceptionally high occupancy of 27.67%. This indicates a critical and consistent interaction that likely dominates the stabilization of C160 in its binding environment. Additional significant interactions include those between LIG628-Side and ASN361-Main (5.84%), LIG628-Side and ASN339-Side (5.69%), and LIG628-Main

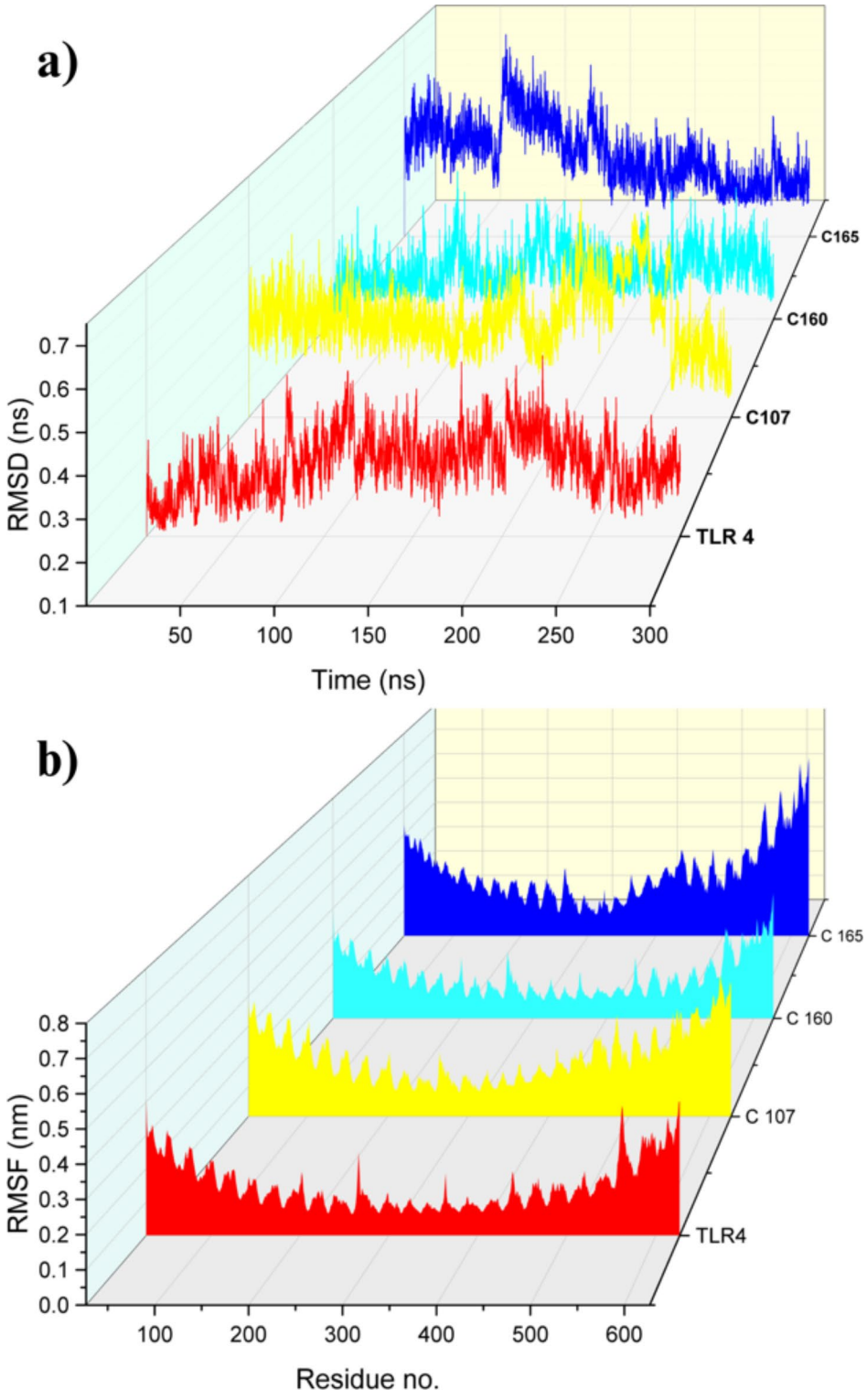

Fig. 8. (**a**) RMSD and (**b**) RMSF obtained from the trajectories of 300ns MD simulations.

and SER360-Side (5.44%), all of which further enhance the stability of the compound. Moderate interactions, such as those involving ASN409, SER360, and ASN383, also contribute to the overall binding stability but to a lesser extent. The numerous low-occupancy interactions observed in C160, while less critical, may still provide additional stabilization through minor contributions.

For compound C165, the hydrogen bond occupancy data suggests a more modest level of interaction compared to C160. The primary interactions involve the side chain of ASN433 with both the main and side chains of LIG628, with occupancies of 2.10% and 1.60%, respectively. These interactions, while not as strong

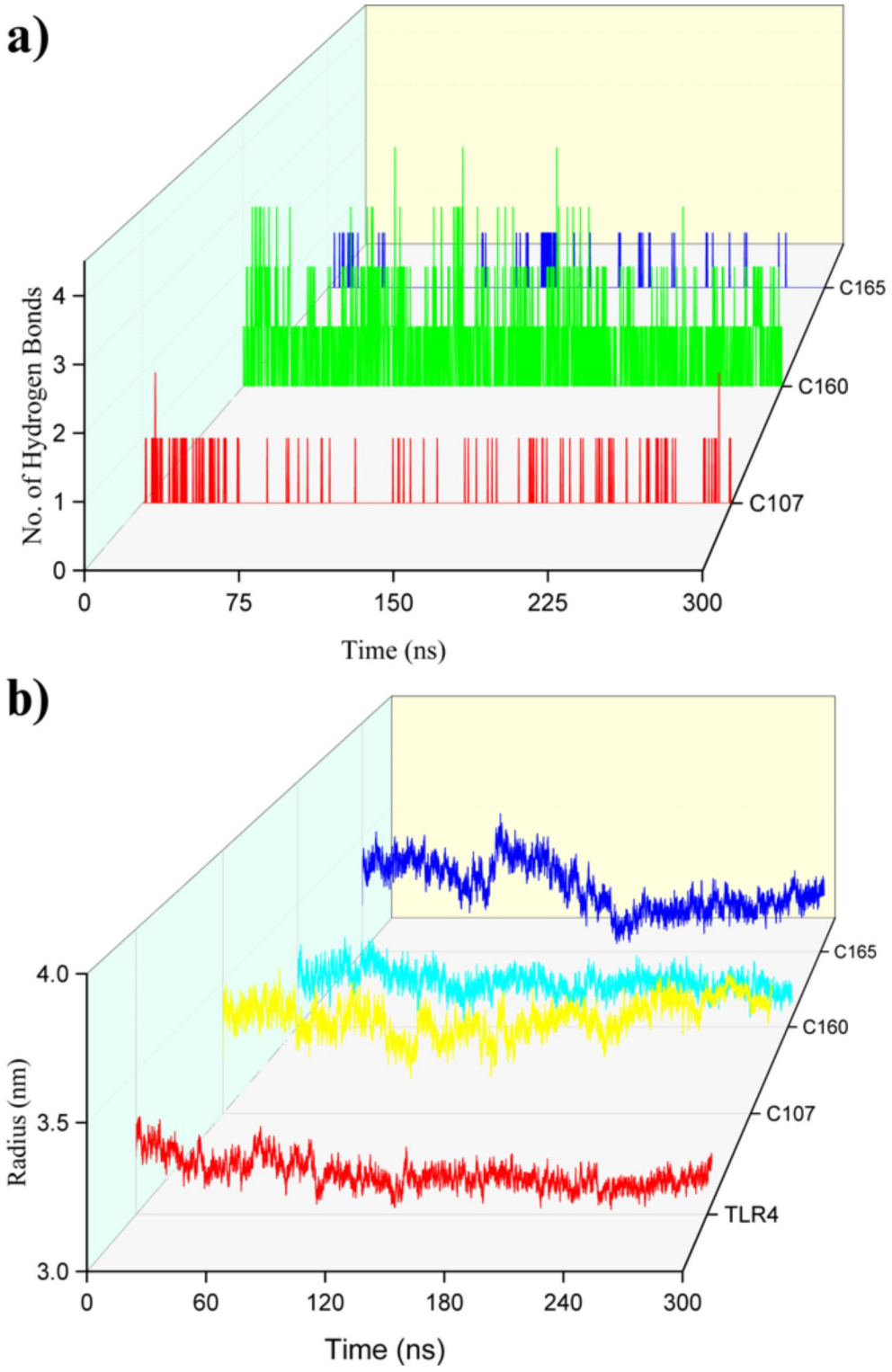

Fig. 9. **a** Number of hydrogen bonds, and **b** radius of gyration analysis plots of TLR4 with C106, C160 and C165 formed during 300 ns MD simulations.

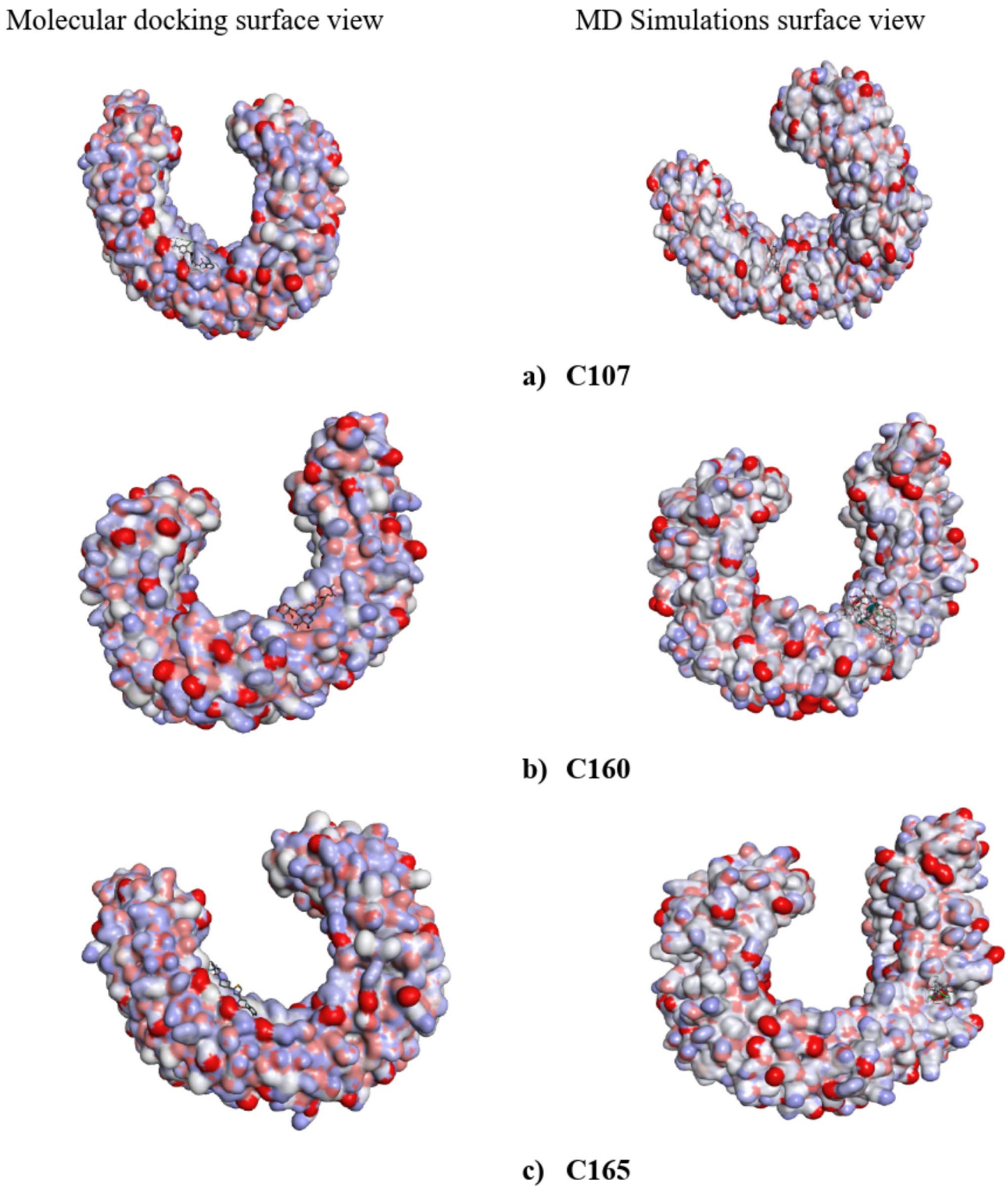

Fig. 10. Surface view of molecular docking and MD Simulations **a** C107 with active site region of TLR4 protein, **b** C160 with active site region of TLR4 protein, **c** C165 with active site region of TLR4 protein.

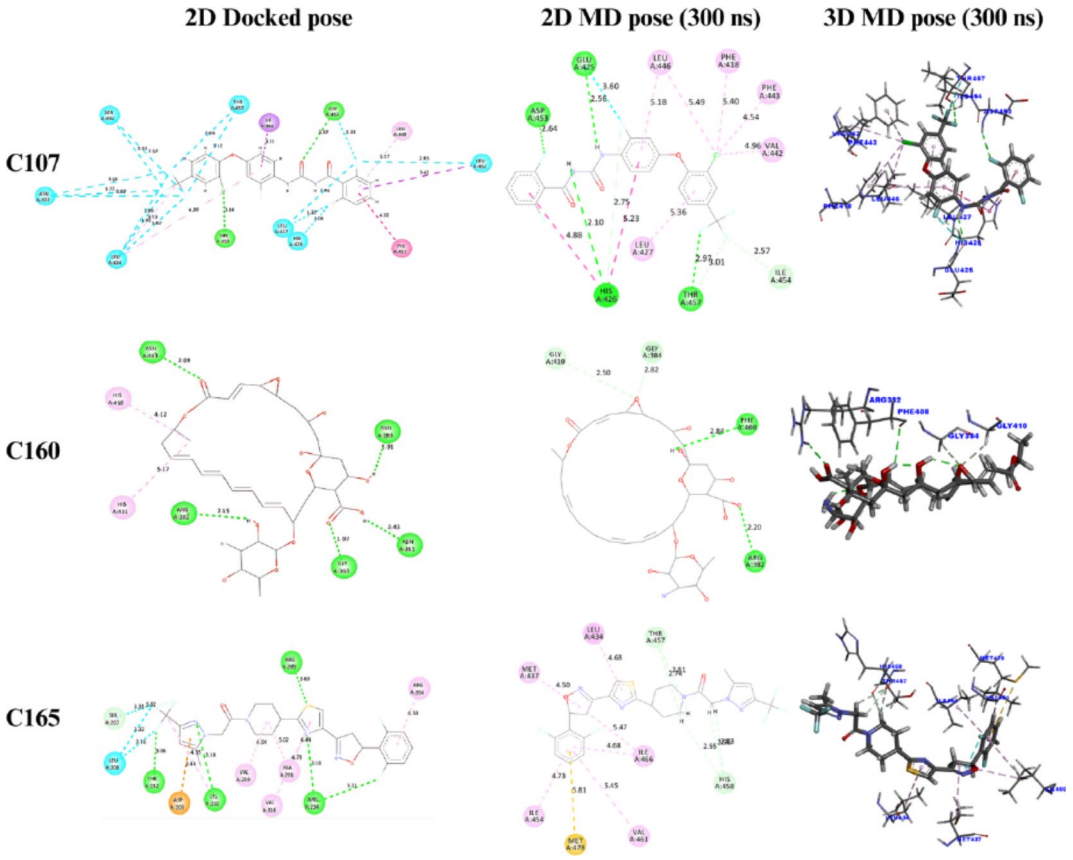

Fig. 11. 2D and 3D representations of docked and MD poses of C107, C160 and C165 with 3FXI.

as those seen in C160, are likely important for the stabilization of C165 within the binding site. The limited number of significant interactions and the absence of high-occupancy bonds suggest that C165 may be less stable compared to C160, but possibly more stable than C107 due to these moderately consistent interactions.

Density functional theory (DFT) calculations of promising pesticides

From a computational perspective, using DFT has developed into an essential approach for estimating the electronic and quantum behavior of molecules[50]. These calculations assist in estimating the stability, enthalpy of formation, and polarity of the compound by computing the energies of the optimised geometry. Due to its exceptional precision and efficiency, DFT has become one of the most widely used techniques for determining electronic structures[51]. Here, these calculations were employed in analysing the structural properties of all three compounds.

Frontier molecular orbitals (HOMO and LUMO) are essential in quantum chemistry, offering key insights into molecular behaviour, properties, and reactivity[52]. The HOMO is the highest energy orbital that contains electrons, making it an electron donor. The lowest energy orbital, or LUMO, on the other hand, is an electron acceptor since it has the ability to take electrons. These HOMO, LUMO and optimized geometry are obtained through DFT calculations are illustrated in Fig. 12. The thermodynamic parameters of C107, C160 and C165 are computed in Table 3. The dipole moment (μ) is frequently used to determine the polarity of the molecules. It assesses how charge fractions are distributed among molecules. Molecules' solubility in water as well as their ability to combine with other solvents can both be affected by their polarity[53]. C107 exhibited highest dipole moment of 12.014129 Debye, indicating highly polar and soluble molecule than C160 and C165. Moreover, the optimization energy was also noted for all three compounds. The optimization energy of C160 (-2318.301 Hartree) was the highest as compared with C107 and C160.

Table 4 displays the energies of HOMO and LUMO which are the important parameters for determining chemical reactivity and selectivity. The energy gaps were determined for HOMO and LUMO orbitals of all three compounds i.e. C107, C160 and C165. The energy gap between the FMOs indicates the structure's kinetic stability. Generally, large energy gaps indicate hard, stable and less reactive molecules whereas small energy gaps indicate soft, less stable and reactive molecule [54,55]. The E_{HOMO}-E_{LUMO} energy gap of C165 (-4.680 eV) was the largest, corresponding to hard molecule with high stability and low chemical reactivity whereas the molecule with the smallest energy gap was C160 (-3.401 eV), suggesting a soft molecule with high chemical reactivity and low stability.

Compound	Donor	Acceptor	Occupancy
C107	THR457-Side	LIG628-Side	1.10%
	LIG628-Side	GLU425-Main	4.10%
	ASP453-Main	LIG628-Side	0.75%
	LEU427-Main	LIG628-Side	0.25%
	LEU434-Main	LIG628-Side	0.15%
	LIG628-Main	HIS426-Side	0.30%
C160	ARG382-Side	LIG628-Side	27.67%
	LIG628-Main	ASN361-Main	1.20%
	LIG628-Side	ARG382-Main	0.10%
	LIG628-Side	ASN409-Main	4.90%
	SER360-Side	LIG628-Side	1.20%
	LIG628-Side	ASN361-Main	5.84%
	LYS362-Side	LIG628-Side	0.75%
	ASN365-Side	LIG628-Main	0.40%
	LIG628-Main	ASN383-Main	0.45%
	ASN433-Side	LIG628-Side	0.05%
	LIG628-Main	SER360-Main	3.05%
	SER360-Side	LIG628-Main	4.65%
	LIG628-Main	SER360-Side	5.44%
	LIG628-Side	SER360-Side	0.95%
	LIG628-Side	ASN383-Main	0.05%
	LYS362-Side	LIG628-Main	0.95%
	LIG628-Main	ASN339-Side	1.20%
	LIG628-Side	ASN339-Side	5.69%
	LIG628-Side	PHE408-Main	0.25%
	LIG628-Side	SER360-Main	1.25%
C165	ASN433-Side	LIG628-Side	1.60%
	ASN433-Side	LIG628-Main	2.10%

Table 2. Hydrogen bond occupancy percentage for C107, C160 and C165.

Physiochemical descriptors of the pesticides

The HOMO and LUMO energies are crucial parameters for determining molecular reactivity, including chemical reactivity descriptors[38]. The HOMO and LUMO values have been used to perform various other calculations, such as determining softness (s), chemical potential (μ), chemical hardness (η), global electrophilicity index (ω) and electronegativity (χ). Electronegativity measures a molecule's ability to attract electrons, with higher χ values indicating a stronger tendency and capacity to attract electrons[56,57]. Chemical potential is the quantity of energy that is either released or absorbed as a result of a change in a species' population[58]. The chemical hardness of a molecule indicates its resistance to the distribution of electron density and helps in understanding the molecular stability whereas softness is a key factor in determining the reactivity of a molecule. Chemical hardness quantifies the resistance to the polarization of electron density on atoms in a system[58,59]. Electrophilicity serves as a significant indicator of reactivity, allowing for a quantitative assessment of a molecule's electrophilic character[60–62]. The physiochemical descriptors of all three compounds are summarized in Table 4. The most electronegative and electrophilic compound was determined to be C107, suggesting its potential to attract and accept electrons (most likely to interact with nucleophiles). Greater polarizability of a species corresponds to higher softness or lower hardness [63–65]. All three compounds showed increased softness and decreased hardness, indicating greater chemical reactivity and lower stability. The order of increasing softness is C165 < C107 < C160 while the order of increasing hardness is C160 < C107 < C165. The low values of the chemical potential of studied molecules indicate stability. This means these molecules cannot break down into the elements from which they were initially formed. It is less likely for molecules with higher negative values of chemical potential to vary their chemical and/or physical states than those with large positive values[66]. Here, C107 was having highest negative chemical potential value of -0.167 Hartree/particle, suggesting that this compound/molecule will not be able to alter its states.

Post MD simulations analysis

The Density Functional Theory (DFT) studies of ligands C107, C160, and C165 post-MD simulations provide significant insights into their electronic properties and potential interactions with the 3FXI protein. The visual representations of the HOMO and LUMO for these ligands (Fig. 13) reveal crucial information about their chemical reactivity and stability. Table 5 mentions the electronic energy and dipole moment of the ligands post 300 ns MD simulations at the binding pocket of the protein. The optimization energies and dipole moments

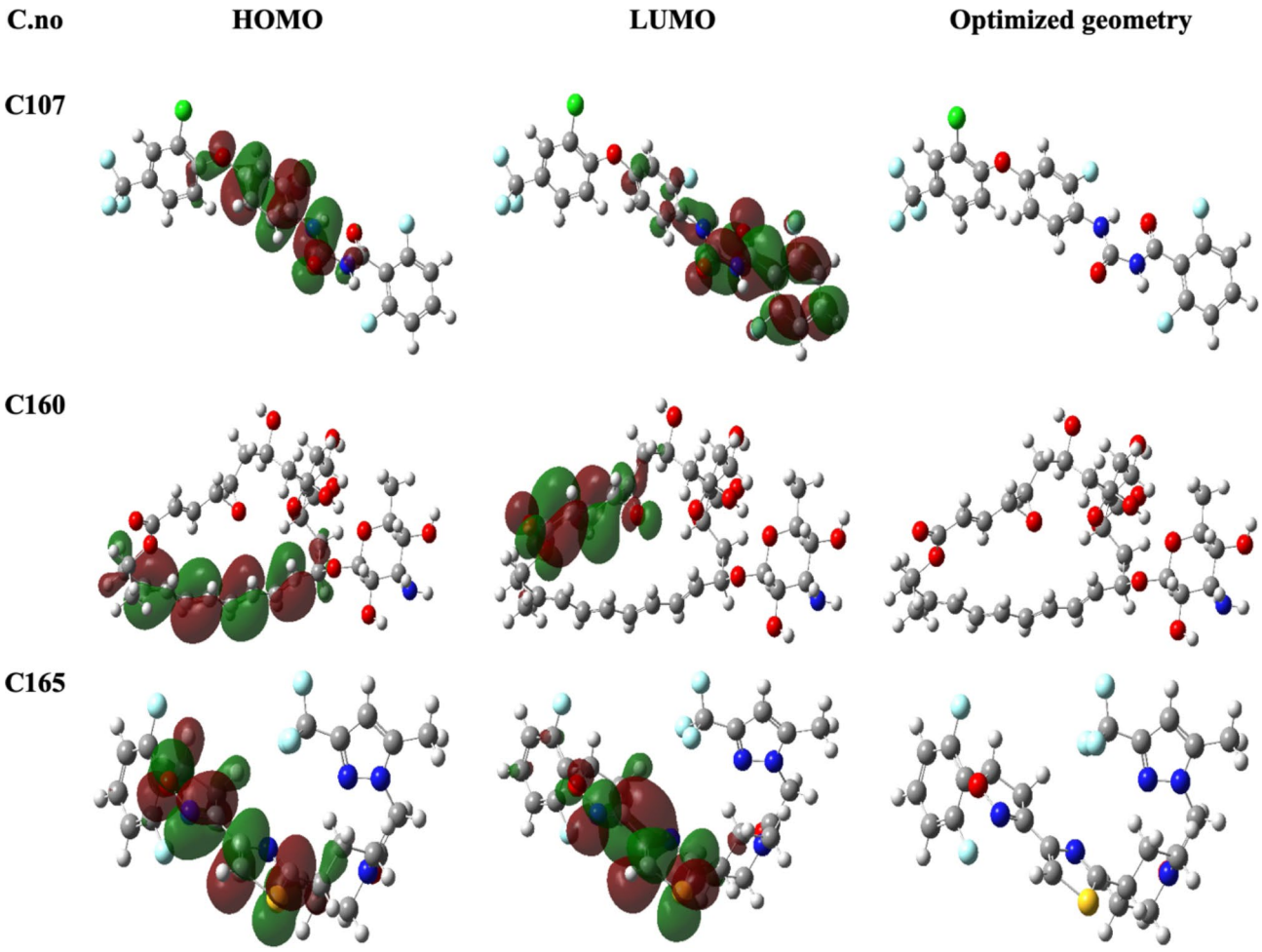

Fig. 12. Visual representation of HOMO, LUMO orbitals and optimized geometry of C107, C160 and C165.

C.no	Optimization Energy (Hartree)	Sum of electronic and zero-point Energies (Hartree per particles)	Sum of electronic and thermal Energies (Hartree per particles)	Sum of electronic and thermal Enthalpies (Hartree per particles)	Sum of electronic and thermal Free Energies (Hartree per particles)	Dipole Moment (Debye)
107	-2201.360829	-2201.071710	-2201.043500	-2201.042555	-2201.136879	12.014129
160	-2318.301570	-2317.518659	-2317.470722	-2317.469778	-2317.601261	7.046643
165	-2249.337167	-2248.895704	-2248.862738	-2248.861794	-2248.966360	10.890072

Table 3. Computed thermodynamic parameters of the C107, C160 and C165.

C.no	E_{HOMO} (Hartree/particle)	E_{LUMO} (Hartree/particle)	$\Delta E (E_{HOMO}-E_{LUMO})$ (Hartree/particle)	$\Delta E (E_{HOMO}-E_{LUMO})$ (eV)	Chemical potential (μ) (Hartree/particle)	Electronegativity (χ) (Hartree/particle)	Hardness (η) (Hartree/particle)	Global electrophilicity index (ω) (Hartree/particle)	Softness (s) (Hartree/particle)
107	-0.249	-0.086	-0.163	-4.435	-0.167	0.167	0.081	0.172	6.172
160	-0.201	-0.076	-0.125	-3.401	-0.138	0.138	0.062	0.153	8.064
165	-0.239	-0.067	-0.172	-4.680	-0.153	0.153	0.086	0.136	5.813

Table 4. Calculated HOMO, LUMO energies and physiochemical descriptors.

indicate that C165 has the highest dipole moment (13.679147 Debye), suggesting a higher polarity which could enhance its interaction with the 3FXI protein through dipole-dipole interactions.

The computed physiochemical descriptors (Table 6) show that C160 has the smallest HOMO-LUMO gap (0.11486 Hartree/particle or 3.1254 eV), indicating it is the most chemically reactive among the three ligands.

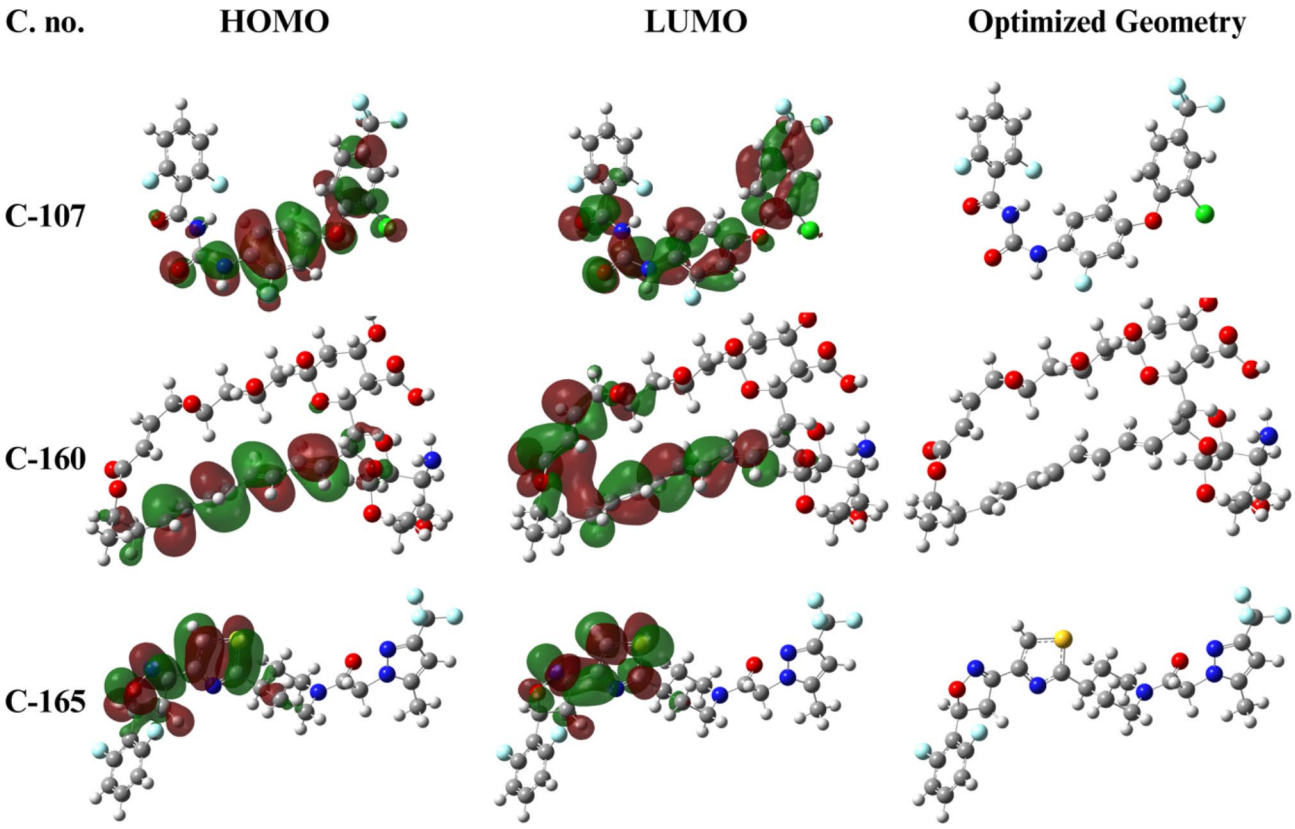

Fig. 13. Visual representation of HOMO, LUMO orbitals and optimized geometry of C107, C160 and C165 post-MD simulations.

C.no	Optimization Energy (Hartree)	Dipole Moment (Debye)
107	-2200.759	6.561
160	-2317.499	5.594
165	-2248.722	13.679

Table 5. Computed thermodynamic parameters of the C107, C160 and C165 post 300ns MD simulation's.

C.no	E_{HOMO} (Hartree/particle)	E_{LUMO} (Hartree/particle)	$\Delta E (E_{HOMO}-E_{LUMO})$ (Hartree/particle)	$\Delta E (E_{HOMO}-E_{LUMO})$ (eV)	Chemical potential (μ) (Hartree/particle)	Electronegativity (χ) (Hartree/particle)	Hardness (η) (Hartree/particle)	Global electrophilicity index (ω) (Hartree/particle)	Softness (s) (Hartree/particle)
107	-0.2308	-0.0576	-0.1732	-4.7135	-0.1442	0.1442	0.0866	0.1200	5.7730
160	-0.1859	-0.0710	-0.1148	-3.1254	-0.1285	0.1285	0.0574	0.1437	8.7062
165	-0.2313	-0.0610	-0.1703	-4.6340	-0.1461	0.1461	0.0851	0.1254	5.8719

Table 6. Calculated HOMO, LUMO energies and physiochemical descriptors post 300 ns MD simulations.

In contrast, C107 and C165 have larger gaps (0.17322 Hartree/particle or 4.7135 eV and 0.1703 Hartree/particle or 4.6340 eV, respectively), suggesting higher stability[58]. The physiochemical descriptors further elucidate the reactivity and stability of the ligands. The chemical potential (μ) and electronegativity (χ) values are relatively similar across the ligands, indicating comparable tendencies to attract electrons. However, the hardness (η) and softness (s) values highlight differences in their resistance to deformation and reactivity. C160, with the highest softness value, is the most reactive, while C107 and C165 are more resistant to electronic deformation. The DFT calculations post-MD simulations reveal that C160 is the most chemically reactive ligand, while C165, with its high dipole moment, may have stronger interactions with the 3FXI protein.

The comparison of DFT calculations for ligands C107, C160, and C165 pre- and post-MD simulations reveals significant changes in their electronic properties and potential interactions with the 3FXI protein. Pre-MD, the optimization energies for C107, C160, and C165 were −2201.360829 Hartree, -2318.301570 Hartree, and −2249.337167 Hartree, respectively. Post-MD, these energies slightly increased due to the protein environment. Notably, C165's dipole moment increased from 10.890072 Debye pre-MD to 13.679147 Debye post-MD, suggesting enhanced polarity and stronger protein interactions.

The HOMO-LUMO gaps (ΔE) also changed. Pre-MD, C160 had the smallest gap (0.125 Hartree/particle or 3.401 eV), indicating high reactivity. Post-MD, this gap decreased further to 0.11486 Hartree/particle (3.1254 eV), reinforcing its reactivity. Conversely, C107 and C165 showed slight increases in their HOMO-LUMO gaps post-MD, suggesting increased stability. The chemical potential (μ) and electronegativity (χ) values remained consistent, but the hardness (η) and softness (s) values highlighted differences in electronic deformation resistance and reactivity. C160, with the highest softness value post-MD, remained the most reactive, while C107 and C165 became more resistant to deformation.

NCI analysis (post MD simulation)

RDG isosurface plot is a powerful tool for visualizing and analyzing the non-covalent interactions within a molecular system, providing insights into the nature, location, and strength of these interactions. The blue region refers to the attractive interactions, typically associated with H-bonds or other strong non-covalent attractive interactions, and the green region is for weak van der Waals interactions or steric clashes. The red area corresponds to strong repulsive interactions due to steric repulsion between atoms[67,68]. Figure 14 shows the non-covalent interactions and RDG scatter graph of C107, C160, and C165. The RDG plot for C107 shows a balance between attractive (hydrogen bonding), weak van der Waals, and repulsive interactions. The presence of strong blue regions suggests that C107 forms significant hydrogen bonds or other non-covalent interactions with the amino acids in the system. Meanwhile, the red regions indicate areas where steric repulsion might be significant, possibly due to the proximity of certain atoms. The RDG scatter plot for C160, like C107, reveals a combination of attractive, van der Waals, and repulsive interactions. Differences in the green and red regions might suggest that C160 has a different balance of van der Waals and steric interactions. C165 has fewer attractive interactions in the blue region, which might indicate weaker or fewer hydrogen bonds. The green and red regions are consistent with the other compounds, suggesting similar weak and repulsive interactions[69,70].

Analysis of ADME properties of the pesticides

The three pesticides, C107, C160, and C165, exhibit distinct physicochemical and pharmacokinetic properties that can influence their toxicity and behaviour within biological systems as shown in Table 7. C107, with a molecular weight of 488.77 g/mol, C160 at 665.73 g/mol and C165 at 539.52 g/mol, vary significantly in size, which directly impacts their ability to cross cell membranes and potentially affects their distribution within the body. The number of heavy atoms, ranging from 33 in C107 to 47 in C160, reflects the molecular complexity, which may also influence their solubility and interaction with biological targets. The ability to form hydrogen bonds is represented by the number of H-bond acceptors and donors and it plays a crucial role in the solubility and permeability of these pesticides. C160, with 14 H-bond acceptors and 7 donors, has a more significant potential for water solubility but might face challenges in crossing lipid membranes, compared to C107 and C165, which have fewer acceptors and donors. The topological polar surface area (TPSA) further highlights this difference, with C160 having a TPSA of 230.99 Å², significantly larger than C107 (67.43 Å²) and C165 (100.85 Å²), suggesting that C160 may have lower membrane permeability and potentially reduced bioavailability. The lipophilicity, indicated by the Consensus Log Po/w, reveals that C107 (5.77) and C165 (4.81) are more hydrophobic, which may enhance their ability to permeate cell membranes but could limit their solubility in aqueous environments. Conversely, C160's Log Po/w of -0.52 suggests a more hydrophilic nature, possibly reducing its ability to cross lipid-rich barriers like cell membranes, but enhancing its solubility in biological fluids. The Log S (ESOL) values, indicating solubility, further support this, with C160 being more soluble (-2.92) compared to C107 and C165, which has much lower solubility (-6.69 and −5.82, respectively). All three compounds exhibit low gastrointestinal (GI) absorption, which could limit their effectiveness and bioavailability when administered orally. None of the pesticides are permeant to the blood-brain barrier (BBB), reducing concerns about central nervous system toxicity. However, their interactions with transport proteins and metabolic enzymes vary, as C107 and C165 are substrates for P-glycoprotein (P-gp), potentially limiting their intracellular concentrations. Additionally, C107 and C165 inhibit multiple cytochrome P450 enzymes (CYP2C19, CYP2C9, CYP2D6, and CYP3A4 in C165), raising the risk of drug-drug interactions and altered metabolic profiles, which could influence their toxicity. Skin permeability, as indicated by Log Kp, is notably low for all three compounds, suggesting that dermal exposure may not be a significant route of toxicity. According to Lipinski's Rule of Five, C107 and C165 each have one violation, while C160 has three, indicating potential challenges in oral bioavailability, particularly for C160. The bioavailability score further underscores these differences, with C107 and C165 having a moderate score of 0.55, while C160 has a much lower score of 0.17, indicating that C160 may have the least oral bioavailability. Overall, the physicochemical properties of these pesticides suggest that C160, with its higher molecular weight, larger polar surface area, and multiple violations of Lipinski's rules, may have the lowest bioavailability and possibly reduced systemic toxicity, but could still pose risks through specific pathways. In contrast, C107 and C165, with their higher lipophilicity and enzyme inhibition potential, may have more pronounced interactions within the body, influencing their toxicity profiles and necessitating careful consideration of their pharmacokinetic behaviour.

The DFT calculations provided critical insights into the electronic properties of the pesticides C107, C160, and C165, which are essential for understanding their reactivity, stability, and potential interactions with biological targets like TLR4. Specifically, the energy difference (ΔE) between HOMO and LUMO, along with

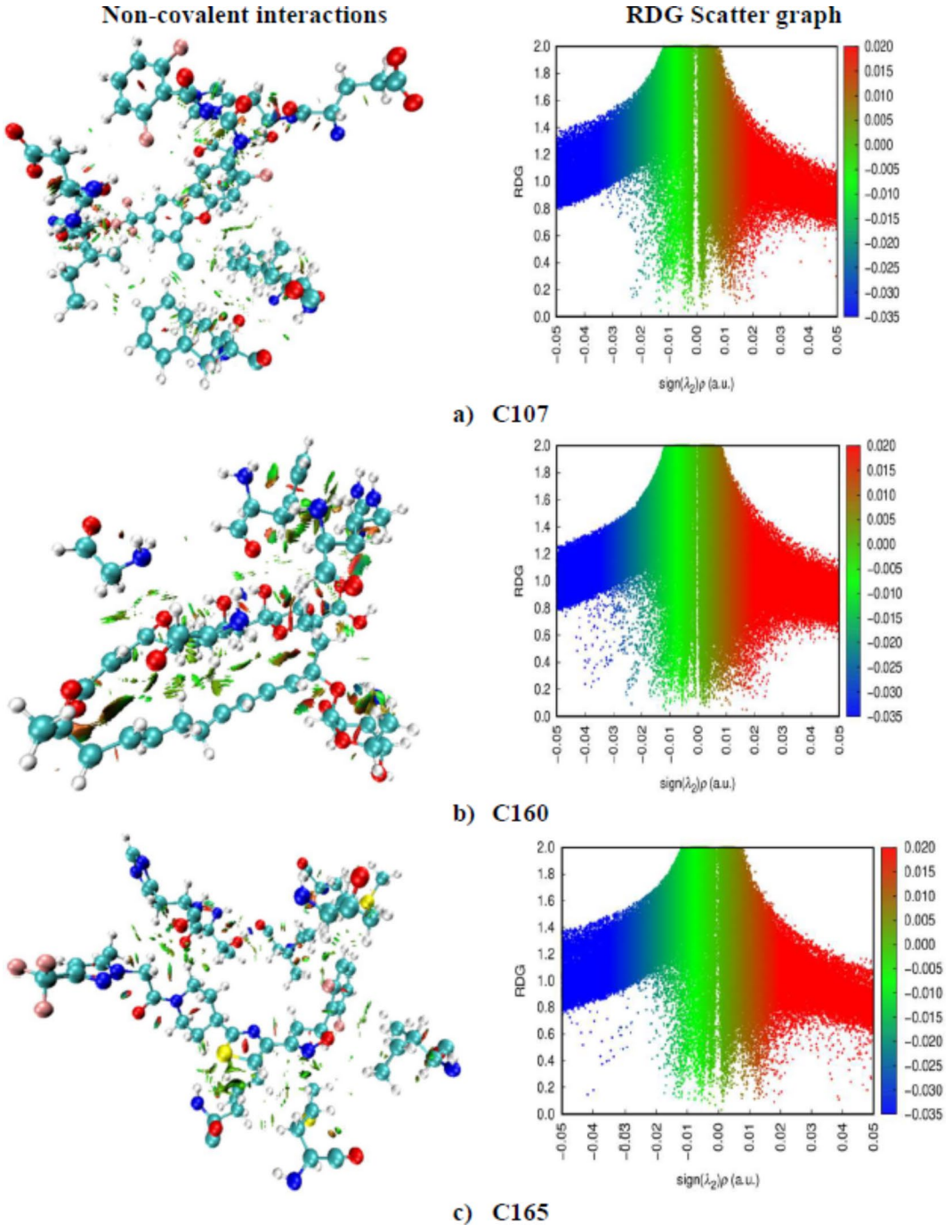

Fig. 14. Non-covalent interactions and RDG scatter graph of **a** C107, **b** C160, and **c** C165.

parameters like chemical potential (μ), electronegativity (χ), hardness (η), and global electrophilicity index (ω), are key indicators of the chemical reactivity and stability of these compounds. The compound C107 shows moderate global electrophilicity (0.172 Hartree) and moderate softness (6.172 Hartree), suggesting a balanced reactivity. The ADME profile shows a high molecular weight (488.77 g/mol), which might affect its GI absorption, and it does have some CYP enzyme inhibition activity, suggesting possible drug-drug interactions. However, its bioavailability score is relatively high (0.55). C160 exhibits the highest electrophilicity (0.153 Hartree) and softness (8.064 Hartree), C160 is the most reactive, which could correlate with stronger biological activity but also a potential for toxicity. The ADME profile, however, shows several violations of Lipinski's rule, a low bioavailability score (0.17), and poor GI absorption, indicating that despite its reactivity, C160 may face significant challenges as a drug candidate. C165 has a ΔE of 0.172 Hartree or 4.680 eV and moderate global electrophilicity (0.136 Hartree), suggesting it is reactive and stable. Its ADME profile indicates a high molecular weight (539.52 g/mol) and some CYP enzyme inhibition, similar to C107, but also a moderate bioavailability score (0.55), albeit with some challenges related to metabolism.

Physiochemical properties	C107	C160	C165
Molecular weight	488.77 g/mol	665.73 g/mol	539.52 g/mol
Number of heavy atoms	33	47	37
Number of H-bond acceptors	9	14	10
Number of H-bond donors	2	7	0
TPSA	67.43 Å²	230.99 Å²	100.85 Å²
Consensus Log Po/w	5.77	-0.52	4.81
Log S (ESOL)	-6.69	-2.92	-5.82
GI absorption	Low	Low	Low
BBB permeant	No	No	No
P-gp substrate	Yes	No	Yes
CYP1A2 inhibitor	No	No	No
CYP2C19 inhibitor	Yes	No	No
CYP2C9 inhibitor	Yes	No	Yes
CYP2D6 inhibitor	Yes	No	Yes
CYP3A4 inhibitor	No	No	Yes
Log Kp (skin permeation)	-4.84 cm/s	-11.32 cm/s	-6.46 cm/s
Lipinski	Yes; 1 violation: MLOGP>4.15	No; 3 violations: MW>500, NorO>10, NHorOH>5	Yes; 1 violation: MW>500
Bioavailability Score	0.55	0.17	0.55
Physiochemical space for oral bioavailability	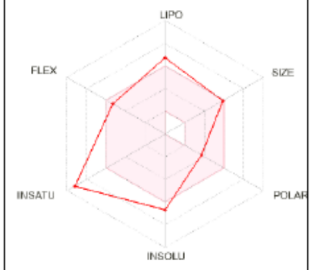	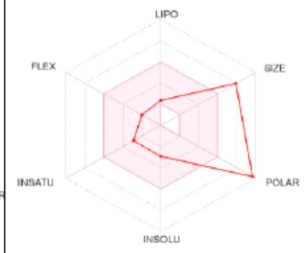	

Table 7. Physiochemical parameters of compounds obtained through ADME studies.

Conclusion

The study provides important insights into the molecular interactions between selected pesticides and the Toll-like receptor 4 (TLR4) protein, which may contribute to cardiovascular toxicity. By employing molecular docking and molecular dynamics simulations, the binding mechanisms of pesticides to TLR4 were studied, revealing how these interactions could potentially disrupt the receptor's function. Our findings highlight specific pesticide-receptor interactions that may play a vital role in triggering inflammatory responses, which are linked to cardiovascular damage. Molecular docking studies andMD simulations were conducted to determine the binding affinities, interactions, and stability of the protein-ligand complexes. Among the pesticides analysed, C160 exhibited the best binding affinity of -8.2 kcal/mol. Both C107 and C165 exhibited a binding affinity of -8.0 kcal/mol. Subsequent MD simulations showed that all the complexes were comparatively more stable than the native protein itself. From PCA analysis, the major structural variations upon ligand binding were observed while DFT calculations offered valuable insights into the reactivity, stability and polarity of compounds. Additionally, the physicochemical properties were evaluated through ADME studies. The results indicated violations of Lipinski parameters. Overall, this analytical study provides valuable insights into pesticide-induced cardiovascular toxicity and may aid researchers in developing effective strategies to mitigate these effects.

Data availability

Data will be provided from the corresponding authors on justified request of reader.

Received: 8 July 2024; Accepted: 7 October 2024
Published online: 18 October 2024

References

1. Tudi, M. et al. Agriculture development, pesticide application and its impact on the environment. *Int. J. Environ. Res. Public. Health*. **18**, 1112 (2021).
2. Rani, L. et al. An extensive review on the consequences of chemical pesticides on human health and environment. *J. Clean. Prod.* **283**, 124657 (2021).
3. Vellingiri, B. et al. Neurotoxicity of pesticides – A link to neurodegeneration. *Ecotoxicol. Environ. Saf.* **243**, 113972 (2022).

4. El-Nahhal, Y. & El-Nahhal, I. Cardiotoxicity of some pesticides and their amelioration. *Environ. Sci. Pollution Res. 2021*. **28:33** (28), 44726–44754 (2021).
5. Sánchez-Alarcón, J. et al. A systematic review of studies on genotoxicity and related biomarkers in populations exposed to pesticides in Mexico. *Toxics 2021*. **9**, 272 (2021).
6. de Teixeira, J. R. Embryotoxic effects of pesticides in zebrafish (Danio rerio): Diflubenzuron, pyriproxyfen, and its mixtures. *Toxics*. **12**, 160 (2024).
7. Zago, A. M. et al. Global Public Health Pesticide exposure and risk of cardiovascular disease: A systematic review. (2020). https://doi.org/10.1080/17441692.2020.1808693
8. Le Quilliec, E., Fundere, A., Al-U'datt, D. G. F. & Hiram, R. Pollutants, including organophosphorus and organochloride pesticides, may increase the risk of cardiac remodeling and atrial fibrillation: a narrative review. *Biomedicines*. **11**, 2427 (2023).
9. Sampurna, B. P. et al. Cardiac rhythm and molecular docking studies of ion channel ligands with cardiotoxicity in zebrafish. *Cells 2019*. **8**, 566 (2019).
10. Wu, Y. et al. Developmental toxicity, immunotoxicity and cardiotoxicity induced by methidathion in early life stages of zebrafish. *Pestic Biochem. Physiol.* **194**, 105526 (2023).
11. Saputra, F. et al. The effect of the pyrethroid pesticide fenpropathrin on the cardiac performance of zebrafish and the potential mechanism of toxicity. *Biology (Basel)*. **12**, 1214 (2023).
12. Peri, F. & Piazza, M. Therapeutic targeting of innate immunity with toll-like receptor 4 (TLR4) antagonists. *Biotechnol. Adv.* **30**, 251–260 (2012).
13. Gawali, B., Sridharan, V., Krager, K. J., Boerma, M. & Pawar, S. A. TLR4—A Pertinent Player in Radiation-Induced Heart Disease? *Genes* **14**, 1002 (2023).
14. Gu, J., Guo, L., Hu, J., Ji, G. & Yin, D. Potential adverse outcome pathway (AOP) of emamectin benzoate mediated cardiovascular toxicity in zebrafish larvae (Danio rerio). *Sci. Total Environ.* **900**, 165787 (2023).
15. Honegr, J. et al. Rational design of novel TLR4 ligands by in silico screening and their functional and structural characterization in vitro. *Eur. J. Med. Chem.* **146**, 38–46 (2018).
16. Honegr, J. et al. Rational design of a new class of toll-like receptor 4 (TLR4) tryptamine related agonists by means of the structure- and ligand-based virtual screening for vaccine adjuvant discovery. *Molecules* **23** (2018). https://doi.org/10.3390/molecules23010102
17. Murgueitio, M. S. et al. Enhanced immunostimulatory activity of in silico discovered agonists of Toll-like receptor 2 (TLR2). *Biochim. Biophys. Acta (BBA) Gen. Subj.* 1861, 2680–2689 (2017).
18. Farhadi, T., Ovchinnikov, R. S. & Ranjbar, M. M. In silico designing of some agonists of toll-like receptor 5 as a novel vaccine adjuvant candidates. *Netw. Model. Anal. Health Inf. Bioinf.* **5**, 31 (2016).
19. Švajger, U. et al. Novel toll-like receptor 4 (TLR4) antagonists identified by structure- and ligand-based virtual screening. *Eur. J. Med. Chem.* **70**, 393–399 (2013).
20. Smith, M. et al. Trial Watch: Toll-like receptor agonists in cancer immunotherapy. *OncoImmunology* **7** (2018). https://doi.org/10.1080/2162402X.2018.1526250
21. Alderson, M. R., McGowan, P., Baldridge, J. R. & Probst, P. TLR4 agonists as immunomodulatory agents. *J. Endotoxin Res.* **12**, 313-319 (2006).
22. Shafaghi, M. et al. Immunoinformatics-aided design of a new multi-epitope vaccine adjuvanted with domain 4 of pneumolysin against Streptococcus pneumoniae strains. *BMC Bioinform.* **24**, 67 (2023).
23. Chen, N. Y., Li, C. P. & Huang, H. F. Synthesis, antitumor evaluation and computational study of thiazolidinone derivatives of dehydroabietic acid-based B ring-fused-thiazole. *Mol. Divers.* **28**, 875-888 (2024).
24. Ikenohuchi, Y. J. et al. A C-type lectin induces NLRP3 inflammasome activation via TLR4 interaction in human peripheral blood mononuclear cells. *Cell. Mol. Life Sci.* **80**, 188 (2023).
25. Pérez-Regidor, L. et al. Small molecules as toll-like receptor 4 modulators drug and in-house computational repurposing. *Biomedicines* 10, (2022).
26. Anwar, M. A., Panneerselvam, S., Shah, M. & Choi, S. Insights into the species-specific TLR4 signaling mechanism in response to Rhodobacter sphaeroides lipid a detection. *Sci. Rep.* **5**, 7657 (2015).
27. de Oliveira, A. A., Faustino, J., de Lima, M. E., Menezes, R. & Nunes, K. P. Unveiling the interplay between the TLR4/MD2 complex and HSP70 in the human cardiovascular system: a computational approach. *Int. J. Mol. Sci.* **20**, 3121 (2019).
28. Vila-Casahonda, R. G., Lozano-Aponte, J. & Guerrero-Beltrán, C. E. HSP60-Derived peptide as an LPS/TLR4 modulator: an in silico approach. *Front. Cardiovasc. Med.* **9**, 731376 (2022).
29. Pence, H. E. & Williams, A. ChemSpider: an Online Chemical Information Resource. *J. Chem. Educ.* **87**, 1123–1124 (2010).
30. Morris, G. M. et al. AutoDock4 and AutoDockTools4: automated docking with selective receptor flexibility. *J. Comput. Chem.* **30**, 2785–2791 (2009).
31. Baroroh, S., Muscifa, U., Destiarani, Z. S., Rohmatullah, W., Yusuf, M. & F. G. & Molecular interaction analysis and visualization of protein-ligand docking using Biovia Discovery Studio Visualizer. *Indones. J. Comput. Biol. (IJCB)*. **2**, 22 (2023).
32. Patil, S., Patil, A., Molecular Docking, P. & V. &, A useful approach of Drug Discovery on the basis of their structure. *Asian J. Pharm. Res.* 191–195. https://doi.org/10.52711/2231-5691.2023.00036 (2023).
33. Benjamin, I. et al. Antimalarial potential of naphthalene-sulfonic acid derivatives: molecular electronic properties, vibrational assignments, and in-silico molecular docking studies. *J. Mol. Struct.* **1264**, 133298 (2022).
34. Yadav, S. et al. Analytic and in Silico methods to understand the interactions between Dinotefuran and Haemoglobin. *Chem. Biodivers.* **e202400495**https://doi.org/10.1002/CBDV.202400495 (2024).
35. Raman, A. P. S. et al. In silico evaluation of binding of 2-deoxy-D-glucose with Mpro of nCoV to Combat COVID-19. *Pharm. 2022*. **14**, 135 (2022).
36. Singh, M. B. et al. A comparative study of 5- fluorouracil, doxorubicin, methotrexate, paclitaxel for their inhibition ability for Mpro of nCoV: molecular docking and molecular dynamics simulations. *J. Indian Chem. Soc.* **99**, 100790 (2022).
37. Vishvakarma, V. K. et al. Pyrrolothiazolones as potential inhibitors for the nsP2B-nsP3 protease of Dengue Virus and their mechanism of synthesis. *ChemistrySelect*. **4**, 9410–9419 (2019).
38. Kumar, D. et al. Understanding the binding affinity of noscapines with protease of SARS-CoV-2 for COVID-19 using MD simulations at different temperatures. *J. Biomol. Struct. Dyn.* **39**, 2659–2672 (2021).
39. Babu Singh, M. et al. An in Silico investigation for acyclovir and its derivatives to fight the COVID-19: molecular docking, DFT calculations, ADME and td-molecular dynamics simulations. *J. Indian Chem. Soc.* **99**, 100433 (2022).
40. Shukla, R. & Tripathi, T. Molecular dynamics simulation of protein and protein-ligand complexes. *Comput. Aided Drug Des.* 133–161. https://doi.org/10.1007/978-981-15-6815-2_7/FIGURES/8 (2020).
41. Alka, Vishvakarma, V. K., Yadav, S., Singh, P. & Jain, P. In vitro, in silico, ADME and theoretical analysis of Mn(II) and Co(II) complexes derived from methyl-(Z)-N′-carbamothioylcarbamohydrazonate Schiff Base ligand. *Chem Biodivers* 20, e202300042 (2023).
42. Radwan, H. A. et al. Design, synthesis, in vitro anticancer and antimicrobial evaluation, SAR analysis, molecular docking and dynamic simulation of new pyrazoles, triazoles and pyridazines based isoxazole. *J. Mol. Struct.* **1264**, 133312 (2022).
43. Rani, A. et al. Computational insights into chromene/pyran derivatives: Molecular docking, ADMET studies, DFT calculations, and MD simulations as promising candidates for Parkinson's disease. *Chem. Biodivers.* **e202400920**https://doi.org/10.1002/CBDV.202400920 (2024).

44. Singh Babu, M. et al. In silico study for acyclovir and its derivatives against Mpro of nCoV: Temperature dependent molecular dynamics simulations (2022). https://doi.org/10.21203/RS.3.RS-1250241/V1
45. Gheidari, D., Mehrdad, M. & Bayat, M. Synthesis, docking, MD simulation, ADMET, drug likeness, and DFT studies of novel furo[2,3-b]indol-3a-ol as promising Cyclin-dependent kinase 2 inhibitors. *Sci. Rep. 2024 14:1* 14, 1–16 (2024).
46. Haider, S., Barakat, A. & Ul-Haq, Z. Discovery of potential chemical probe as inhibitors of CXCL12 using ligand-based virtual screening and Molecular Dynamic Simulation. *Molecules* **25**, 4829 (2020).
47. Hendam, A., Al-Sadek, A. F. & Hefny, H. A. Molecular dynamic simulation of Neurexin1α mutations associated with mental disorder. *J. Mol. Neurosci.* **72**, 2252–2272 (2022).
48. Anjum, F. et al. Bioactive phytoconstituents as potent inhibitors of casein kinase-2: dual implications in cancer and COVID-19 therapeutics. *RSC Adv.* **12**, 7872–7882 (2022).
49. Kumari, A., Mittal, L., Srivastava, M., Pathak, D. P. & Asthana, S. Conformational characterization of the Co-activator binding site revealed the mechanism to achieve the bioactive state of FXR. *Front. Mol. Biosci.* **8**, 658312 (2021).
50. Abu-Dief, A. M. et al. Synthesize, structural inspection, stoichiometry in solution and DFT calculation of some novel mixed ligand complexes: DNA binding, biomedical applications and molecular docking approach. *J. Mol. Liq.* **399**, 124422 (2024).
51. Raman, A. P. S. et al. Exploring the molecular interactions between acyclovir and hormones: insights from density functional theory calculations. *ChemistrySelect* 8, e202303320 (2023).
52. Abu-Izneid, T. et al. Density functional theory (DFT), molecular docking, and xanthine oxidase inhibitory studies of dinaphthodiospyrol S from *Diospyros kaki* L. *Saudi Pharm. J.* **32**, 101936 (2024).
53. Raman, A. P. S. et al. DFT calculations, molecular docking and SAR investigation for the formation of eutectic mixture using thiourea and salicylic acid. *J. Mol. Liq.* **362**, 119650 (2022).
54. Moyeenul Huq, A. K. M. et al. Phenolic compounds of Theobroma cacao L. show potential against dengue RdRp protease enzyme inhibition by In-silico docking, DFT study, MD simulation and MMGBSA calculation. *PLoS One*. **19**, e0299238 (2024).
55. Quayum, S. T. et al. Exploring the effectiveness of flavone derivatives for treating liver diseases: utilizing DFT, molecular docking, and molecular dynamics techniques. *MethodsX*. **12**, 102537 (2024).
56. Smith, D. A., Beaumont, K., Maurer, T. S. & Di, L. Clearance in drug design. *J. Med. Chem.* **62**, 2245–2255 (2019).
57. Yousaf, M. A., Basheera, S. & Sivanandan, S. Inhibition of Monkeypox Virus DNA polymerase using Moringa oleifera Phytochemicals: computational studies of drug-Likeness, molecular docking, molecular dynamics simulation and density functional theory. *Indian J. Microbiol.* 1–18. https://doi.org/10.1007/S12088-024-01244-3/FIGURES/5 (2024).
58. Aslam, M. et al. Study the solubility of pharmaceutical ingredients and their eutectic mixtures: an in-depth density functional theory and molecular dynamics simulations approaches. *J. Mol. Liq.* **397**, 124070 (2024).
59. Singh, H., Singh, A., Banipal, T. S., Singh, P. & Bahadur, I. Temperature and concentration dependent physicochemical interactions of L-ascorbic acid in aqueous LiCl solution: experimental and theoretical study. *Colloids Surf. Physicochem. Eng. Asp.* **623**, 126672 (2021).
60. Saouli, S. et al. Synthesis, spectroscopic characterization, crystal structure, DFT studies and biological activities of new hydrazone derivative: 1-(2,5-bis((E)-4-isopropylbenzylidene)cyclopentylidene)-2-(2,4-dinitrophenyl) hydrazine. *J. Mol. Struct.* **1213**, 128203 (2020).
61. Zouchoune, B. Theoretical investigation on the biological activities of ginger and some of its combinations: an overview of the antioxidant activity. *Struct. Chem.* **32**, 1659–1672 (2021).
62. Allal, H., Nemdili, H., Zerizer, M. A. & Zouchoune, B. Molecular structures, chemical descriptors, and pancreatic lipase (1LPB) inhibition by natural products: a DFT investigation and molecular docking prediction. *Struct. Chem.* **35**, 223–239 (2024).
63. Kumar, A., Kumari, K., Singh, S., Bahdur, I. & Singh, P. Noscapine anticancer drug designed with ionic liquids to enhance solubility: DFT and ADME approach. *J. Mol. Liq.* **325**, 115159 (2021).
64. Kumar, A. et al. Promising iron(II) complexes of curcumins: designing, density functional theory, and molecular docking. *J. Phys. Org. Chem.* **34**, e4196 (2021).
65. Aslam, M. et al. Impact of functional group positioning in the anion of ionic liquids on aqueous solubility: a study through DFT calculations. *Ionics (Kiel)*. **30**, 875–887 (2024).
66. Abu-Melha, S. et al. Multicomponent synthesis, DFT calculations and molecular docking studies of novel thiazolyl-pyridazinones as potential antimicrobial agents against antibiotic-resistant bacteria. *J. Mol. Struct.* **1234**, 130180 (2021).
67. Yadav, S. et al. Insights into DES Stability and reactivity with carboxylic acids: a computational approach. *J. Comput. Biophys. Chem.*https://doi.org/10.1142/S2737416524500443 (2024).
68. Farrokhi, R. A. & Shahverdizadeh, G. H. Hirshfeld surface analyses, NCI–RDG and effect of surfactant on the size of Co3O4 nanostructures obtained from cobalt(II) nano-complex. *J. Mol. Struct.* **1294**, 136400 (2023).
69. Boukabcha, N. et al. Spectral investigation, TD-DFT study, Hirshfeld surface analysis, NCI-RDG, HOMO-LUMO, chemical reactivity and NLO properties of 1-(4-fluorobenzyl)-5-bromolindolin-2,3dione. *J. Mol. Struct.* **1285**, 135492 (2023).
70. Kandasamy, S. et al. In silico, theoretical biointerface analysis and in vitro kinetic analysis of amine compounds interaction with acetylcholinesterase and butyrylcholinesterase. *Int. J. Biol. Macromol.* **185**, 750-760 (2021).

Acknowledgements

Authors convey thanks to Prof B. Jayaran, Incharge, SCFBio, Indian Institute of Technology, Delhi, India for the using the facilities.

Author contributions

Iona Massey, Sandeep Yadav, Mohd. Aslam, Ayushi Prajapat, Durgesh Kumar – Collected the data, literature, draft writing, performed calculations, Analysis, Software used; Bhaskara Nand, Garima Pandey, Chandrabhan Verma, Akram AlFantazi, Prashant Singh, Kamlesh Kumari – Conceptualization, Analysis, visualization; and finalization of the manuscript.

Funding

Not Applicable.

Declarations

Competing interests

The authors declare no competing interests.

Ethical approval

Not applicable.

Clinical trails
Not applicable.

Additional information
Supplementary Information The online version contains supplementary material available at https://doi.org/10.1038/s41598-024-75527-6.

Correspondence and requests for materials should be addressed to K.K., P.S. or A.A.

Reprints and permissions information is available at www.nature.com/reprints.

Publisher's note Springer Nature remains neutral with regard to jurisdictional claims in published maps and institutional affiliations.